Type-II Superlattice Avalanche Photodiodes

BY

JUN HUANG
B.S., Nanjing University of Science and Technology, China, 2009
M.S., University of Illinois at Chicago, 2012

THESIS

Submitted as partial fulfillment of the requirements
for the degree of Doctor of Philosophy in Electrical and Computer Engineering
in the Graduate College of the
University of Illinois at Chicago, 2015

Chicago, Illinois

Defense Committee:

Vitali Metlushko, Chair
Siddhartha Ghosh, Advisor, Raytheon
Zheng Yang
Mitra Dutta
Christoph Grein, Physics

This thesis is dedicated to my wife Ju Liang, my coming daughter, my parents Duhe Wang and Yuqin Huang, and my sister Lin Huang.

ACKNOWLEDGEMENTS

I would like to express my deepest appreciation to my advisor, Dr. Siddhartha Ghosh. He guided me not only in academic research projects, but also in how to research with an independent thinking. Without his mentorship, this dissertation would not have been possible.

I would like to thank my committee chair Professor Vitali Metlushko, Professor Michael Stroscio, Professor Mitra Dutta and Professor Zheng Yang, for teaching me tremendous knowledge in semiconductor physics and semiconductor fabrication process. I would also thank Professor Christoph Grein for physics theory and simulation discussions which helped me in fundamental knowledge understandings.

I sincerely thank Professor Majeed Hayat from University of New Mexico who built dead space multiplication theory for the gain and excess noise simulations on avalanche photodiodes, based on which I fulfilled novel photodiodes structure design and modeling.

I would also thank Dr. Koushik Banerjee, with whom I worked closely during the stay in UIC. I have learned much of physics device simulations and fabrication from him. Also, I thank Mr. Bob Lajos and Dr. Seyoung An for the semiconductor fabrication help in Nanotechnology Facility at UIC.

I am thankful to my friends Wenbo Mu, Qing Duan, Ke Tang, Weixiang Shao, Ke Xu and all others who embraced my graduate life in Chicago. I thank prof. Sidhhartha Ghosh and the

whole Electrical and Computer Engineering department, UIC for providing financial assistantships, research facilities.

Finally, I would like to acknowledge with gratitude, the love of my family - my wife and my parents. They gave me support and love which kept me going and researching. This dissertation has been made possible because of them.

JH

CONTRIBUTION OF AUTHORS

Chapter 1 is a literature review that introduces the basic knowledge of infrared wave regions, superlattices and avalanche photodiodes. Chapter 2 presents the fabrication techniques that I used for the following chapter devices. Chapter 3 talks about the passivation X-ray spectra examination for superlattice avalanche photodiodes in collaboration with Dr. Koushik Banerjee. Chapter 4 gives the simulation for passivated superlattice avalanche photodiode which I worked closely with Dr. Koushik Benerjee. Chapter 5 represents a published manuscript for which I was the first author and major driver of the research. Chapter 6 gives a conclusion and a possible future work that might be done on superlattice avalanche photodiodes area.

TABLE OF CONTENTS

TABLE OF CONTENTS (continued)

LIST OF TABLES

TABLE PAGE

LIST OF FIGURES

FIGURE PAGE

LIST OF FIGURES (continued)

LIST OF ABBREVIATIONS

AFM	Atomic Force Microscopy
ALD	Atomic Layer Deposition
APD	Avalanche Photodiode
BOE	Buffered Oxide Etch
DEZn	Diethylzinc
DI	De-Ionized
DSMT	Dead Space Multiplication Theory
HRXRD	High Resolution X-Ray Diffraction
IR	Infrared
LWIR	Long Wavelength Infrared
MBE	Molecular Beam Epitaxy
ML	Monolayer
MWIR	Mid Wavelength InfraRed
NFA	Noise Figure Analyzer
PL	PhotoLuminescence
QWIP	Quantum Well Infrared Photodetectors
RHEED	Reflected High-Energy Electron Diffraction
RMS	Root Mean Square
SAM	Separate Absorption and Multiplication

LIST OF ABBREVIATIONS (continued)

SLS	Strained Layer Superlattice
SMU	Source-Monitor Unit
SNR	Signal to Noise Ratio
SNS	Smart Noise Source
SRH	Schokley-Reed-Hall
SWIR	Short Wavelength InfraRed
TAM	Thioacetamide
TEM	Transmission Electron Microscopy
UV	Ultra-Violet
XPS	X-ray Photoelectron Spectroscopy

SUMMARY

Avalanche photodiodes have been widely used in several instrumentation and aerospace applications such as spatial light transmissions, laser range finders and object detections. Avalanche photodiodes operate under relatively higher electric fields to generate new pairs of electron and hole from impact ionization which combines the detection part and amplification part into a single device, leading to an increase of the response speed and sensitivity. Several materials for avalanche photodiodes have been researched for different wavelengths. In infrared region, mercury cadmium telluride has been considered as the industry standard. However, it requires very strict process in the growth due to the high vapor pressure of mercury, higher cut-off wavelength sensitivity from cadmium concentration. In this thesis, type-II superlattice avalanche photodiodes are studied. Type-II III-V superlattice avalanche photodiodes have shown several advantages compared to conventional mercury cadmium telluride photodiodes. It can be tuned to fit different wavelength detections from short wavelength to wide wavelength infrared. Moreover, their band structures can be designed by k.p band theory to discover the better ionization coefficients for electrons and holes resulting in a reduction in the excess noise. Also, it enables a uniform growth on relative larger area with a near mature fabrication process. Therefore, type-II III-V superlattice avalanche photodiodes have been considered as one of the alternate for infrared detection. The excess noise is a key characteristics of avalanche photodiodes because the avalanche process is a stochastic process without the knowledge of the exact location and time that impact ionization happens. The excess noise factor, F, is used to describe this property. In the superlattice related

devices, its gain can be calculated as the first moment while the excess noise factor will be related to its second moment.

In order to achieve great characteristics for superlattice avalanche photodiodes, the bandgap and its electron and hole ionization coefficients have to be designed carefully. To minimize the excess noise factor, a pure or dominant electron or hole initiated multiplication can be applied. Molecular beam epitaxy system is used to grow the superlattice on III-V wavfer. Then, the wafer is diced into several smaller pieces with different areas for comparable characterization. Each sample is patterned with photo lithography and etched by etching solutions. Finally, metal pads are deposited by electron-beam evaporation.

Surface or interface leakage current has been a major issue for avalanche photodiode, especially in infrared wavelength region with a small bandgap. Passivation of the superlattice device with Ammonium sulfide and thioacetamide was carried out, and its surface quality was studied by X-ray Photoelectron Spectroscopy. The study showed that both ammonium sulfide and thiacetamide passivation could actively remove the native oxide at the surface. Thiacetamide passivation combined more sulfur bonds with III-V elements than that of ammonium sulfide. Another X-ray photoelectron spectra of thiacetamide-treated atomic layer deposited zinc sulfide was performed. Different sulfides are generated at the surface of samples only with TAM treatment. It shows that sulfur might have a preference to combine with III-V elements. Sb–S and

As–S bonds disappear while In-S bond gets enhanced, indicating that Indium Sulfide should be the major components at the interface after ZnS deposition.

ATLAS simulation of zinc sulfide, silicon nitride and silicon dioxide passivated superlattice devices was performed to discover the surface current mechanism to compare with that with no passivation. First, superlattice property parameters were filled into a bulk for the compliance of ATLAS software. Second, some minor structure or tunneling mass modification was fulfilled to ensure the accuracy of numerical computation. Third, surface mechanism parameters were fitted to match the experimental results of the same device. Through the analysis of fitted parameters, ZnS passivated avalanche photodiode showed the improvement in all these three aspects (surface recombination, trap density and shunt resistant) which corresponds to a better electrical characteristics from the experiment result. SiO_2 passivated devices surface current also implied negligible surface recombination and traps assisted mechanism. However, there was no significant improvement in shunt leakage current. Si_xN_y passivated devices exhibited a relatively smaller surface recombination velocity and shunt leakage, leaving interface trap density almost unchanged.

Finally, a dual-carrier avalanche photodiode was designed and simulated. The structures have alternate carrier multiplication regions, placed next to a wider electron multiplication region, creating dual-carrier feedback systems. Gain and excess noise factor of these structures were

calculated based on the dead space multiplication theory under uniform electric field. From the simulation, the applied bias can be greatly lowered or the thickness can be shrunk to achieve the same gain from the conventional device. It creates the possibility of integrating dual APDs directly to silicon read-out circuits without the need of high voltage supplies. Also, with low electric field, it can reduce dark currents in linear and dark count in single photon counting applications. The width of the thin region was shown to be the most critical parameter determining the device performance. With that width increasing, both gain and excess noise increase. Since this APD structure includes both electrons and holes to create feedback systems, there will be a reduction in bandwidth, thus resulting in low gain-bandwidth products.

1. INTRODUCTION

1.1 Background

1.1.1 Wien's Displacement Law

In 1893, Wilhelm Wien first applied the law of thermodynamics to electromagnetic radiation, concluding that the wavelength distribution from a thermal radiation of a black body at any temperature has exactly the same shape with that at any other temperature as shown in Figure 1. For instance, human bodies whose temperature is around 300K, the electromagnetic radiation is maximized at wavelength of 9.66 μm according to Wien's Displacement Law [1] from Figure 1.

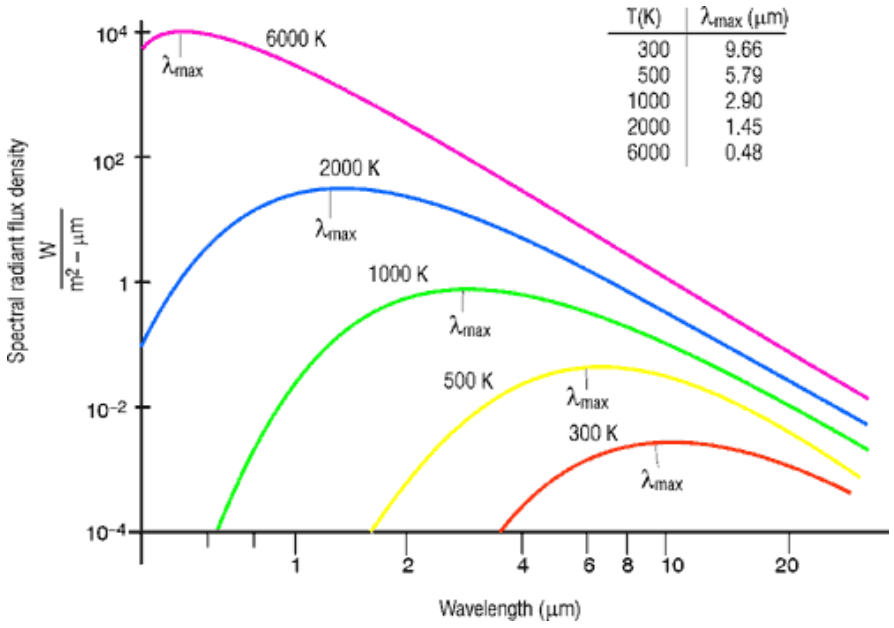

Figure 1 Wien's Displacement Law

1.1.2 Infrared Wave

For electromagnetic spectrum [2] shown in Figure 2, the whole spectrum is separated into different wavelengths or frequencies. What we are studying in this thesis is focused on infrared region which is between visible and microwave spectrum. From Figure 1, low and moderate temperatures have the radiation distribution with most of spectrum including peak lied in the infrared region. Therefore, the radiation of human beings and animals with the peak around 10

μm belongs to infrared wave region. And for this reason, infrared detection has arose huge interest in military and civilian research facilities.

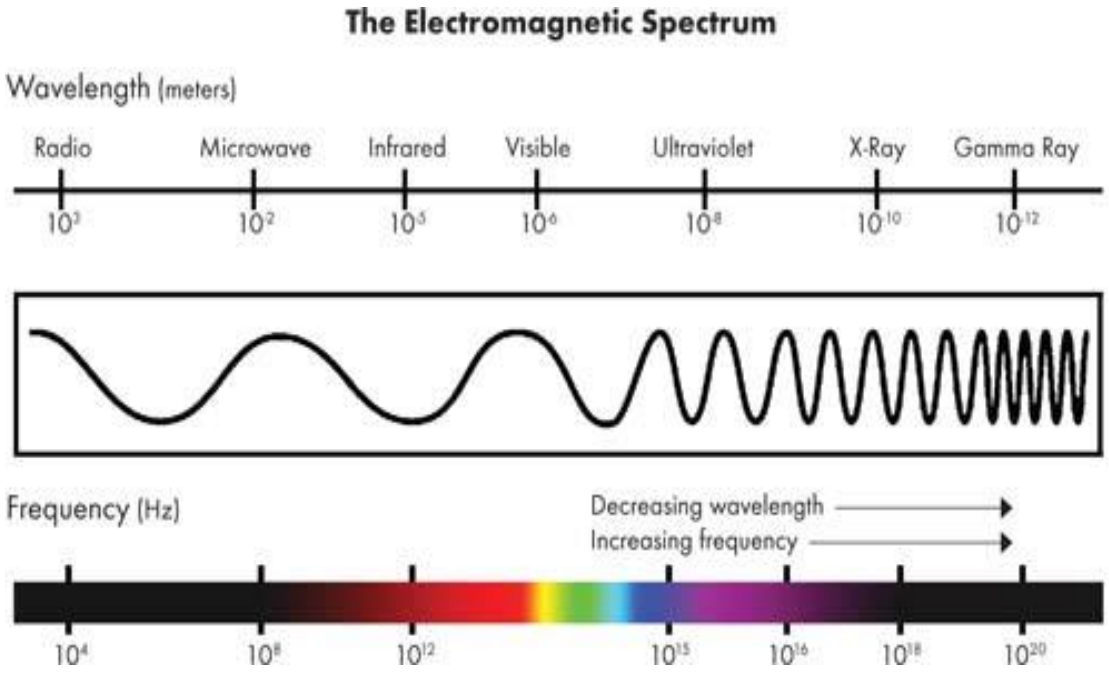

Figure 2 Electromagnetic Spectrum

To be more specific, IR wavelengths can be classified into three windows as shown in Figure 3, short-wave (SW) 0.75 µm- 2.5 µm, mid-wave (MW) 3 µm- 5 µm, and long-wave (LW) 8 µm- 14 µm infrared. There are numerous applications for infrared detection in the field of bioscience and thermal imaging as well as in military. In real situations, some portion of infrared signal can be shrunk due to the environment and atmosphere noise, causing signal to noise ratio (SNR) to be low. To increase SNR, it is better to increase the signal while keeping noise level. Therefore, avalanche photodiodes (APDs) play an important role by combining the detection phase and the gain phase in a single device which can provide an internal gain, also reducing the overall receiver complexity.

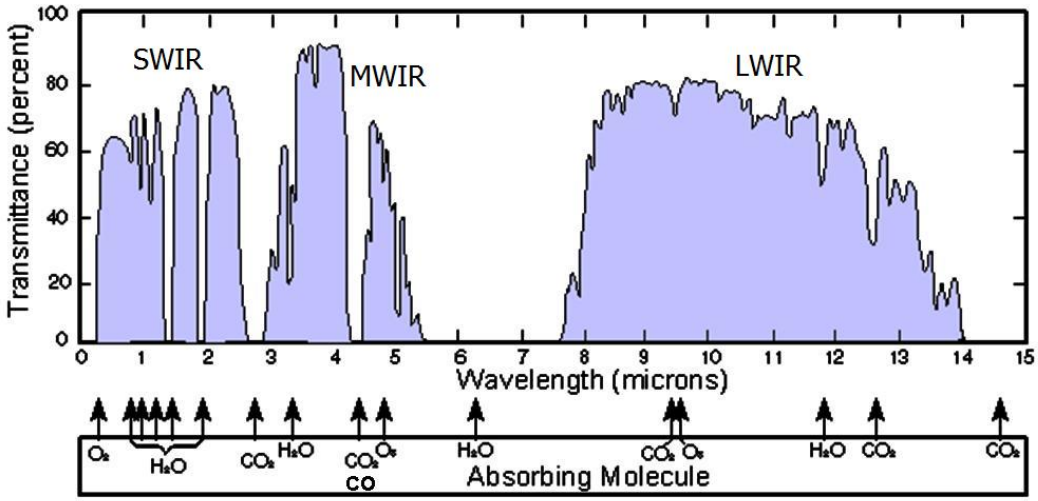

Figure 3 Infrared transmission through atmosphere

1.2 Photodiodes and Avalanche Photodiodes

1.2.1 Photodiodes

A photodiode is a semiconductor device usually formed with a P-N or P-I-N structure, which converts incident electromagnetic radiation into an equivalent electrical signal mostly current. Photons with sufficient energy strike the diode and can generate electron-hole pair carriers. Carriers generated in the depletion region or one diffusion length away from it are swept from the junction by the built-in electric field. If they are collected at the electrical contacts without recombination, an output current will be generated. Others charge carriers outside the depletion region will move randomly. Some will finally enter the depletion region while others recombine

and disappear without touching the depletion region. By varying the semiconductor doping levels and the external bias, the thickness of the depletion region can be increased. Also, an extended depletion region can be realized using a PIN structure under a relative small bias, leading to the increase of the quantum efficiency.

However, for conventional photodiode, since one photon can only generate one electron-hole pair and every carrier has its limited lifetime, it cannot be guaranteed that every carrier will reach the electrical contacts. Thus, it can be only used for high-density photon detection. For low-density photon detection, an internal gain will be required.

1.2.2 Avalanche Photodiodes

Avalanche photodiodes [3] internally amplifies charger carriers with an avalanche process. They have similar P-N or P-I-N structures, but are operated under a much higher reverse bias that can cause impact ionization compared to conventional photodiodes. Under high electric field, photo-carriers can achieve high kinetic energy and have probability to collide with the atomic lattice, knocking out additional carrier pairs. And these secondary carriers can also be accelerated by electric field and get impact ionization, hence the avalanche multiplication. The process of avalanche multiplication in a semiconductor was first reported by McKay [6]. The avalanching mechanism is described in Figure 4. The minimum energy required for a carrier to impact ionize

is called the ionization threshold energy. It mostly depends on the material bandgap and its overall band structure.

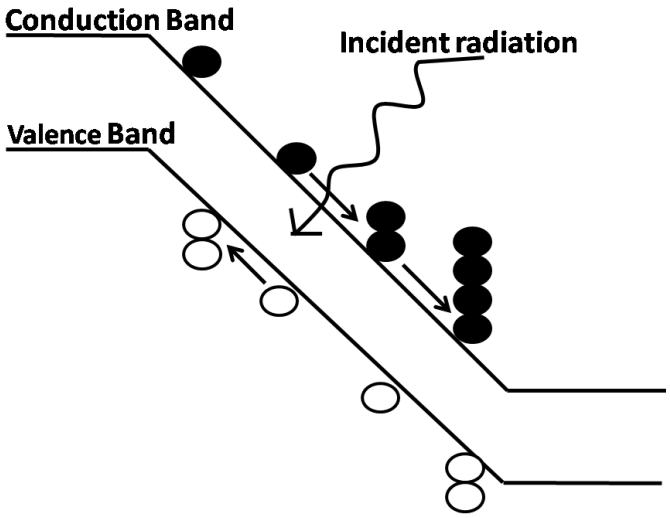

Figure 4 Avalanche mechanism in space domain

Avalanche process is a random process since time and position for carriers to impact inoze are random variables with certain probability distributions. Therefore, this process renders a high frequency noise at the device output, named as excess noise. McIntyre [6] first proposed a model to quantify the excess noise. According to this model, carriers can impact ionize if the local electric field exceeds a critical value. For an electron initiated avalanching process the excess noise factor *F*, a measure of excess factor, is given as,

$$F = kM + (1-k)(2-\frac{1}{M}) \quad (1)$$

where M=gain, $k=\beta/\alpha$, α, β are electron and hole ionization coefficient, respectively. Also, for a hole initiated case, the excess noise factor can be written as

$$F = \frac{1}{k}M + \left(1-\frac{1}{k}\right)(2-\frac{1}{M}) \quad (2)$$

This model implies that the excess noise factor can be minimized when the value of k goes to either too low (close to zero) or too high (close to infinity) which indicates only one of the carriers should dominate the avalanching process. Though this model accurately prescribes the recipe for low excess noise, it fails to accurately quantify excess noise factors in all conditions. McIntyre model assumes that only the local electric field is responsible for impact ionization, completely ignoring the carrier history. However, a newly generated carrier with no or little energy cannot immediately impact ionize even when experiencing a steep electric field. It must accelerate over a minimum distance, depending on the electric field and the ionization threshold energy, before it is enabled to do so. This minimum distance is termed as the dead space which is first experimentally discovered by Anselm et. al. [7], and theoretically modeled and developed by M.M. Hayat [9] and J.S. Marsland [8].

1.2.3 Characteristics of Avalanche Photodiodes

Photodiodes have many characteristics [13] to consider, such as excess noise in the last section. Selected characteristics should be examined based on the requirement of the photodiodes. Some important characteristics are listed below.

1.2.3.1 Operation Range

Based on the requirement of photodiodes, they can be operated and have different sensitivity in different wavelength. The operation range is always around its bandgap. Therefore, material of photodiodes can be selected from its operation range.

1.2.3.2 I-V Characteristics

Among electrical characteristics, I-V Curve is the very important one. From I-V Curve, breakdown voltage and leakage current can be approximated in the dark current curve. Also, combined with light-on curve, the gain of the photdiodes can be estimated.

1.2.3.3 Excess Noise and Signal to Noise Ratio (SNR)

Excess Noise [89] comes from the uncertainty of time and location about impact ionization of the certain carriers. It can describe as a variation or second moment of the mean gain. The larger excess noise is, the more unsteady for the photodiodes.

The SNR of an APD is given by

$$SNR = \frac{(MR_\lambda P_{in})^2}{2qM^2F(R_\lambda P_{in} + I_{darkm})\Delta f + 2qI_{darkum}\Delta f + \frac{4kT}{R_{load}}F_n\Delta f} \quad (3)$$

where P_{in}=incident radiation power, R_λ=responsivity, M=gain, F=excess noise factor, I_{darkm}=dark current through the bulk which gets multiplied similar to the photocurrent, I_{darkum}=dark current at the surface which is not multiplied, k=Boltzmann constant, R_{load}=load resistance, F_n=noise figure of associated circuitry, Δf=bandwidth. For a regular photodiode M=F=1. Maximizing the SNR involves suppressing the dominating noise source or increasing the signal power.

1.2.3.4 Frequency response

The rise and fall time of a photodiode is defined as the time span for the signal to rise from 10% to 90% or fall from 90% to 10%. It can be expressed as frequency response.

$$t_r = \frac{0.35}{f_{3db}} \quad (4)$$

1.3 Materials for Avalanche Photodiodes (APDs)

For the materials of photodiodes, their bandgap should match the incident photon energy. With this criteria, high quantum efficiency can be achieved. If the bandgap is much smaller than the photon energy, no photon can be absorbed and no current will be generated; while if it is much larger, photon will be absorbed at the surface and the charge carriers will be trapped in the surface states. Thus, for longer wave detection region where the wavelength is in the range of 3μm-5μm and 8μm -14μm, the bandgap of the material should be around 0.24eV-0.41eV and 0.088eV-0.155eV according to Planck-Einstein Equation. Figure 5 gives an overview of different materials used for infrared absorption.

$$E = hf = \frac{hc}{\lambda} \tag{5}$$

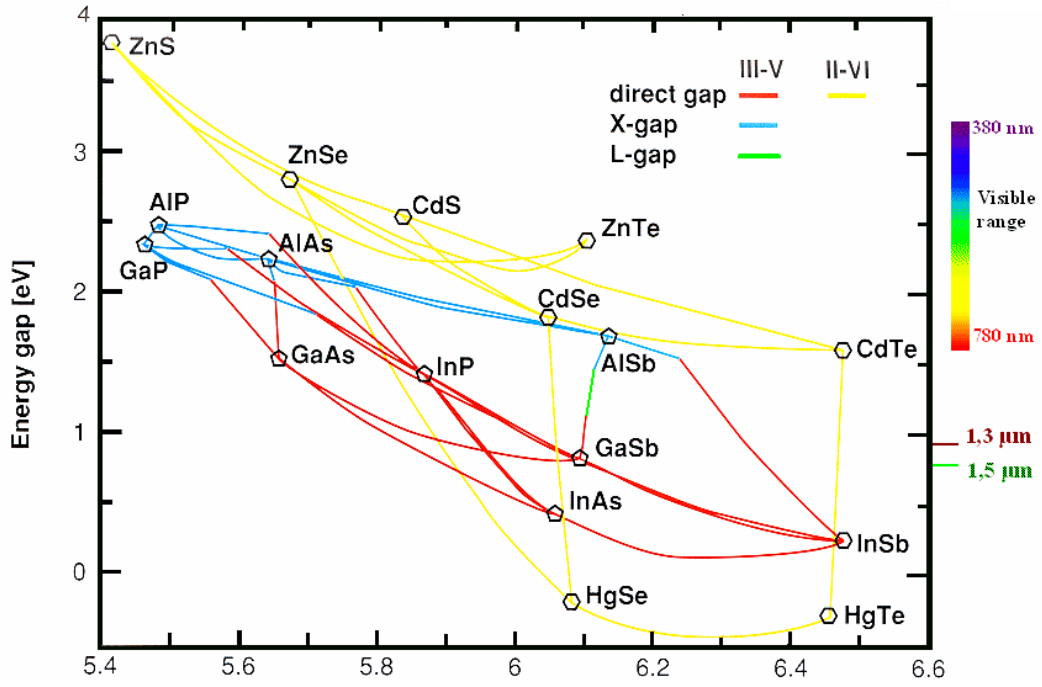

Figure 5 Bandgap of different semiconuctors as a function of lattice constant

1.3.1 Silicon (Si) APDs

Silicon APDs are often used in visible and near IR range with relative low multiplication noise. Nowadays these APDs are very robust with high responsibility and excellent sensitivity. [14]

1.3.2 Germanium (Ge) and Indium gallium arsenide (InGaAs) APDs

Germanium [21] and Indium gallium arsenide [24] APDs can also detect visible to 1500nm wavelength range. However, based on its material natural properties they can be extended for a longer infrared wavelength.

1.3.3 Mercury cadmium telluride (HgCdTe) based APDs

In 1959, Lawson [29] first reported the unprecedented behavior of $Hg_{1-x}Cd_xTe$ in the whole of infrared absorption. Since then it has become the unanimous choice for most of the commercial, traditional and sophisticated longer wavelength infrared detection devices [30] due to its higher absorption coefficients [35], tunable energy bandgap [36], and promising recombination mechanism [37].

However, HgCdTe APDs requires very strict process [38] in the growth due to the high vapor pressure of mercury (Hg), higher cut-off wavelength sensitivity from cadmium (Cd) concentration and hard separation of mercury telluride (HgTe) and cadmium telluride (CdTe).

1.3.4 Superlattice based APDs

To solve the difficulties stated above, several alternate technologies have come up. The most significant technologies are lead salt alloy [45] which is based on IV-VI materials, quantum well infrared photodetectors (QWIP) [48] and type-II strained layer superlattice (SLS) [52] which are based on III-V material. This thesis mainly discusses SLS III-V materials for APD applications.

Superlattice materials have a periodic structure with at least two alternate thin layers with each having a different semiconductor material. Each layer is thin enough (most of them are within several nanometers) that the electronic wave functions can overlap with each other so that a unique band structure can be created whose properties are different that from individual bulks. Unlike a bulk structure in which the band structure is fixed, a superlattice band structure can be tailored through its layer thickness and materials, making it possible for the band structure design. Depend on the heterostructure type of materials in the superlattice, it can be classified as type I, type II and type III. For type I superlattice band structure, the bottom of conduction band of one material and the top of the valence band of the other materials are formed in the same semiconductor layer. For type II, there are no overlap between the conduction band of one material and the valence band of the other, so that electrons and holes can be confined in different layers. For type III, it contains semimetal material.

Figure 6 shows Type II band alignment of InAs/GaSb interface. The conduction band minima of InAs lies 0.15eV below the valence band maxima of GaSb at 300K. The electrons are confined in the InAs quantum well, whereas the holes are confined in the GaSb quantum well. The spatial separation of electrons and holes results in type-II band alignment.

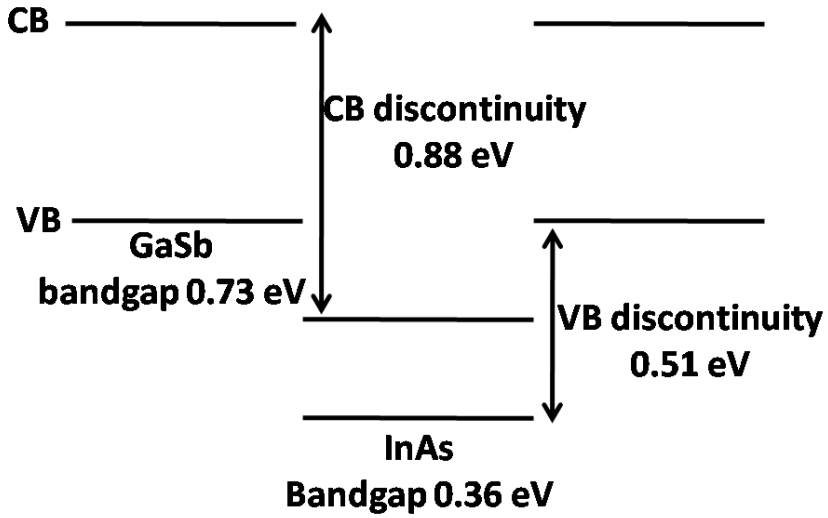

Figure 6 Type II band alignment at InAs/GaSb interface at 77K

For Type II InAs/GaSb superlattices, the bandgaps can be tuned to cover a wider range of IR wavelengths by varying the widths of the layer. Bandgap simulations with a 14 band k.p method is shown in Figure 7. SLS layers can be adjusted not only to control the bandgap as mentioned earlier, but also to engineer the overall bandstructure of the semiconductor material. This can have a significant effect in quantum mechanism by suppressing Auger recombination process especially in p-doped material by eliminating available high energy states for holes. And,

it can be designed to enhance impact ionization by one major carrier which can play an important role in excess noise reduction.

Compared to HgCdTe growth, III-V SLS can be grown with much more uniformity on relatively large GaSb wafers. Also, the fluctuation of the cut-off wavelength is not as sensitive to layers' thicknesses as it is with Cd content for HgCdTe. Mature III-V processing technologies also provide the SLS system an edge over the II-VI system.

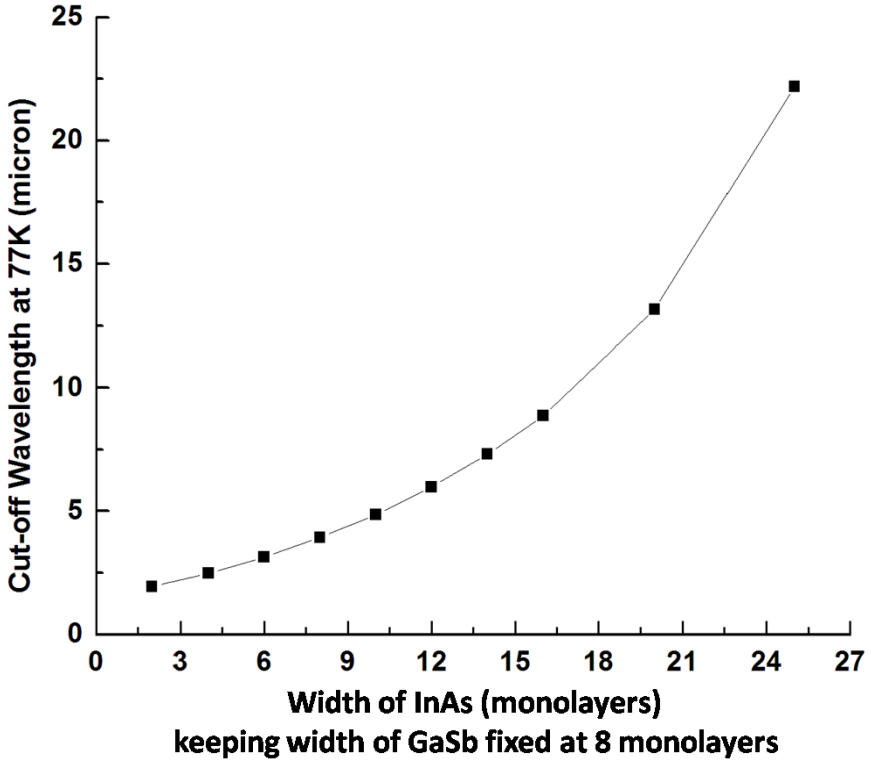

Figure 7 Variation of cut-off wavelength with superlattice composition

1.4 Material Structure Band and Device Software Engineering

1.4.1 Perturbation Theory

In quantum mechanics, electrons always have wave functions that can be described in the following equation where p is its momentum operator, V is the potential, m is the mass and E is its energy. This is Schrodinger Equation.

$$\left(\frac{p^2}{2m} + V\right)\psi = E\psi \tag{6}$$

Bloch went further to prove that the solution for this equation can be written as the following for a crystalline solid, where **k** is the wave vector, n is the band index, u is a periodic function with band index and wave vector.

$$\psi_{n,K}(X) = e^{iK\cdot X}u_{n,K}(X) \tag{7}$$

1.4.2 Modeling and Simulation of APD Strucutre

The dead space multiplication theory (DSMT) can be used for avalanche photodiode gain and excess noise structure simulations since it is more precise compared to conventional models [9]. It assumes that a minimum distance a new generated carrier has to travel along the electric

field before it can impact ionized, and that minimum distance it travels should have the carrier to achieve threshold energy. It will be fully explained and used for structure design in Chapter 5.

Semiconductor device simulation can be done with professional soft wares. Besides getting results from real experiments, professional device software can help simulate the environment and get results as long as we input the materials datasets, build the correct structures, select prominent mechanism. In chapter 4, we will discuss do the inverse engineering to get the underlying prominent mechanism behind the device using the experiment results.

2. FABRICATION OF SUPERPATTICE AVALANCHE PHOTODIOES

Fabrication techniques for III-V superlattices APDs are described in this chapter. Discussion includes an introduction to pure electron and hole APDs, the growth and fabrication of superlattices. Passivation for superlattice photodiodes will be discussed in next Chapter.

2.1 Electron and Hole Avalanche photodiode

To achieve low excess noise factor *F*, impact ionization ratio *k* should be kept low or high, which means only electron or hole impact ionization dominated [97]. In general, it can be achieved by superlattice band structure design which can maximize electron (hole) ionization rate while keeping hole (electron) ionization rate extremely low. Simulation and fabrications of electron and hole avalanche photodiodes with type II strained layer superlattice materials nowadays are realized.

2.2 Growth and Fabrication of Type II InAs/GaSb Strained Layer Superlattice

2.2.1 MBE Growth

Type II InAs/GaSb Superlattices are grown on n-type (Te-doped 10^{17} cm^{-3}) GaSb (1 0 0) substrates with an Oxford VG-80 solid source molecular beam epitaxy (MBE) system. MBE system is one of deposition methods which can allow films to grow epitaxially under ultra high vacuum (~10^{-11} torr) environment. High vacuum environment can prevent the contamination, thus

reducing impurity. VG-80 MBE system consists of a load lock system which can load and unload the substrates without venting the rest of system, a preparation chamber that prepares the substrates with vacuum and heating needs, and two identical growth chambers where films are grown epitaxially on substrates.

Group III source materials (indium, gallium and aluminum) are confined in effusion cells with inert crucibles and can be heated by radiation from resistance heaters. They are also equipped with dual filament which can separate heating of the tip and the base of the cells, thus improving the uniformity of epitaxial growing. Group V source materials (antimony, arsenic) are kept in cracker source which produces dimeric molecules from elemental sources. The crack source for arsenic is valved in order to controls As_2 flux, stabilizing the cell temperature and lowing flux transients. Cell temperatures are monitored by thermocouples to ensure the stability. With the substrate inside the growth chamber, high temperature can desorb surface oxides of GaSb substrates. But, the heating at a higher temperature should be done in a Sb_2 flux environment since group V elements have low vapor pressures, resulting in desorption of Sb. Therefore, substrate temperature is gradually increased to 400°C under ultra-high vacuum and then increased to 550°C under Sb_2 flux. Group-V are adjusted using an ion gauge while Group-III are regulated by the reflected high-energy electron diffraction (RHEED) patterns.

During epitaxial growth, shuttles for different sources are left open and close intermittently. While the Ga (In) shutter is closed, the Sb_2 (AS_2) flux is left open for a limited time, leading to an insertion of additional source of compressive (tensile) strain coming from the mismatch of lattice constant. Strain compensation allows the growth of thick superlattice layers required for superior quantum efficiency of photodiodes. Soak time is carefully and precisely determined to control the thickness of interfacial layers, thus the strain in the grown superlattice structure.

Several techniques such as atomic force microscopy (AFM), transmission electron microscopy (TEM), photoluminescence (PL) and x-ray diffraction (HRXRD) can be used to inspect the quality and properties of the superlattice.

2.2.2 Dicing

The superlattice wafer is diced into 10 mm by 10 mm samples. Several different diameter (50um – 400um) photodiodes are fabricated on each sample. Circular cross sections photodiodes are preferred since square cross sections diodes will have larger leakage current due to sharp edges, leading to premature breakdown.

2.2.3 Patterning, Etching and Deposition

The general fabrication steps are shown in Figure 8. Firstly, after the photo lithography, the etching solution of 20:2:1 deionized (DI) water: hydrogen peroxide (H_2O_2): phosphoric acid (H_3PO_4) were used to etch down the mesa to the bottom layer using 365 nm ultraviolet UV

photolithography. Then, metal contact is deposited by electron beam evaporation. 300 Å titanium (Ti)/ 200 Å platinum (Pt)/ 1000 Å gold (Au) are chosen for contact metals. Gold is used to prevent oxidation of the materials, very stable and conductive. Pt is used to prevent gold to diffuse into other materials especially in high temperature environment. Ti is adhesive to semiconductor surface and good for the ohmic contact with both p- and n-type SLS. After that, a dielectric passivation layer is deposited on top of the sample. Dielectric layer on top of metal contacts is etched down by proper etchant. Finally, gold is deposited to create the pads which are used for probing during electrical measurements. Simple APDs are fabricated after above steps. However, since surface leakage current in LWIR and MWIR will be significantly high compared to its relative operating current. Further techniques of passivation on superlattice APDs are discussed in Chapter 3.

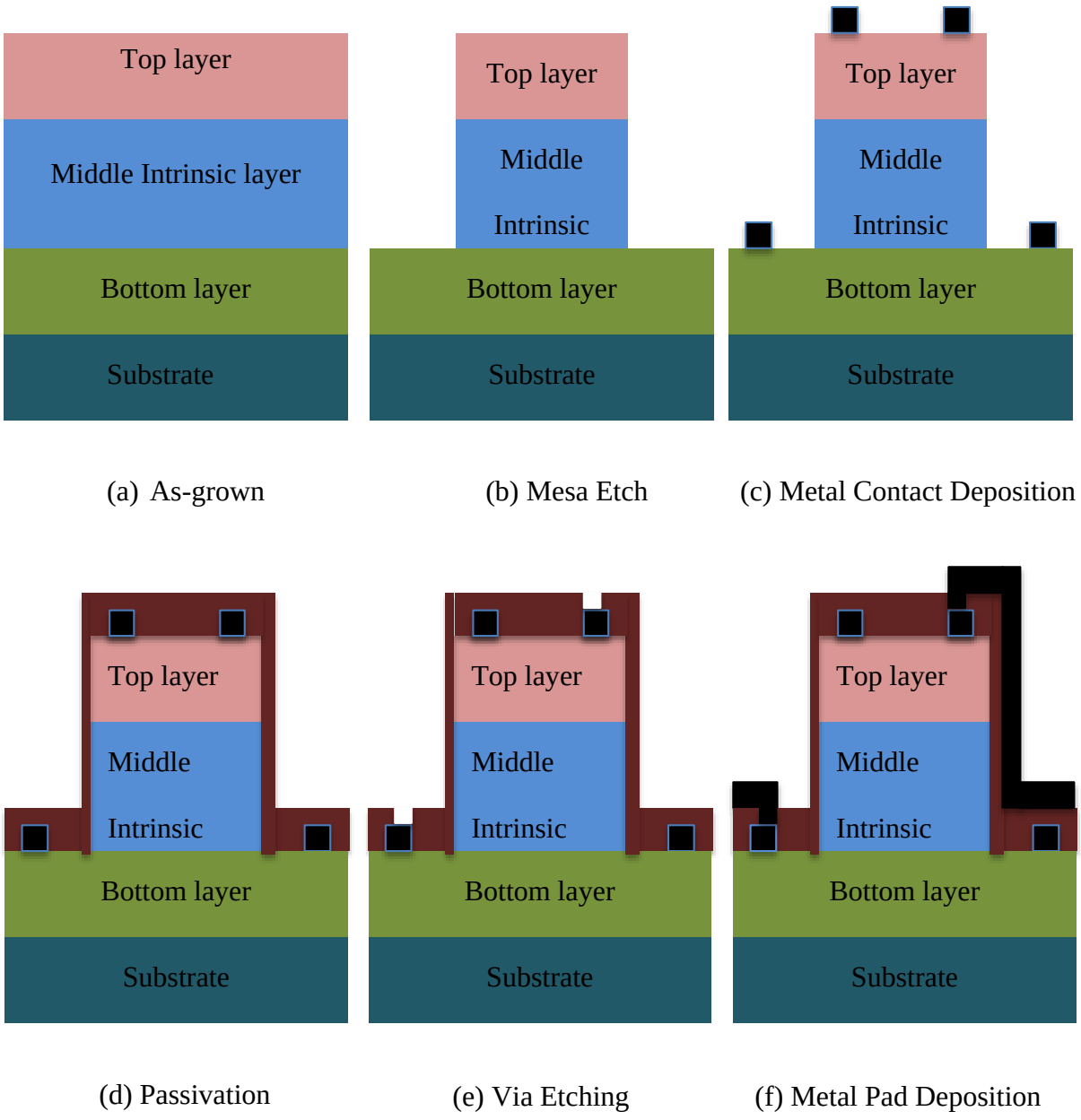

(a) As-grown (b) Mesa Etch (c) Metal Contact Deposition

(d) Passivation (e) Via Etching (f) Metal Pad Deposition

Figure 8 General Fabrication Processes

3. PASSIVATION OF SUPERLATTICE AVALANCHE PHOTODIOES

3.1 Purpose for Passivation

Existence of active states at the surface will bend the band at the surface to maintain the charge neutrality condition. If the surface state is of acceptor (donor) type, it will accept (donate) an electron and will become negatively (positively) charged and as a result a few monolayers underneath the surface will become deficit (rich) of electron and will be charged oppositely. The nature of the surface band bending in equilibrium and non-equilibrium conditions is discussed in [53]. In avalanche photodiode applications, it will initiate a surface plasma breakdown before the junction breakdown. The existence of these surface states will help recombine the photo-generated and multiplication-generated carriers. The stability of larger bandgap insulators (e.g. SiO_2, Si_3N_4, ZnS) at higher electric fields gives them an edge over $(NH_4)_2S$ aqueous solution for passivation for these applications. Along with insulation, carriers experience less effect from the surface due to larger conduction and valence band offset at the passivant-SLS interface. Any sulfur-based aqueous solution might leave the surface with less number of unsaturated recombination centers, but the stability and electrical insulation of the surface passivant at higher electric field and higher band offsets at the passivant-SLS interface are considered critical parameters of interest along with other parameters for avalanche photodiode application. A number of passivation techniques has been applied to LWIR and MWIR superlattices such as silicon-dioxide (SiO_2) [54] , polyimide [55] , SU-8 [56] and ammonium sulfide [$(NH_4)_2S$] [57]. Also, a new surface treatment of

thioacetamide (TAM) with ZnS [61] passivation has shown considerable decrease in diode dark current.

3.2 TAM-treated and $(NH_4)_2S$-treated Superlattice

Chalcogen-based treatment which is the modification of surface with sulfur atoms on III-V materials has been studied by numerous research groups [61]. It was reported that $(NH_4)_2S$ sulfidization can effectively reduce the native oxides and improve surface properties. $(NH_4)_2S$ can actively remove native oxides and create a covalently bonded sulfur layer, leading to the surface leakage current reduction and the impovement of dynamic resistance area product at zero bias. However, $(NH_4)_2S$ solutions can also etch the material surface which might damage the device structures. Therefore, during the surface etching, extra precision is required. In order to maintain good long term stability and prevent the degradation of device performance for SLS detectors and III-V devices, an encapsulating layer on top of the surface has been used [69]. Moreover, a new sulfidization solution with Thioacetamide (TAM) has recently been researched as an effective sulfidizing agent for InAs/GaSb surfaces. It show a great effectiveness since a better electric characteristics has been achieved from TAM-treated devices with lower surface leakage and higher R_0A.

A detailed XPS study on InAs/GaSb SLS photodetectors surface with different passivants were carried out and compared in this chapter. In Figure 9, the comparison of interface sulfur

elements are shown. Peaks centered at 161.3eV and 162.6eV that corresponding to $2p_{1/2}$ and $2p_{3/2}$ from orbital energies of sulfur ($2p_{3/2}$ energies at Ga_2S_3-162.2eV, In_2S_3-162.4eV, Sb_2S_3-161.8eV) are detected. Peaks at 164.8eV corresponding to As_2S_3 was merely observed. It shows that TAM-treated sample exhibits a much stronger sulfidation rather than $(NH_4)_2S$-treated sample.

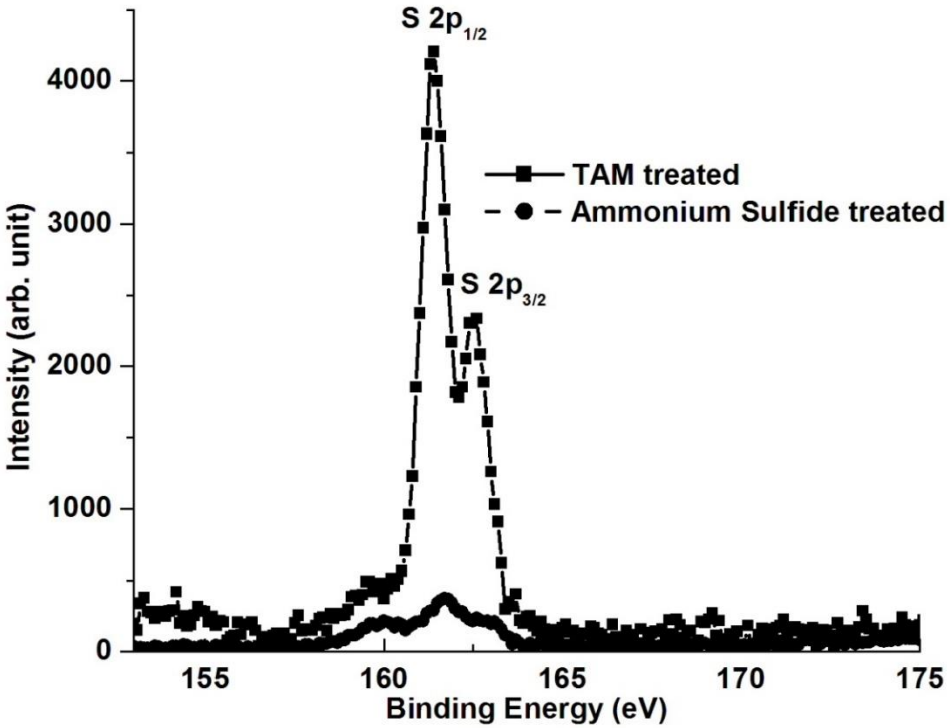

Figure 9 XPS spectra on sulfur elements from TAM- and $(NH_4)_2S$-treated samples

The XPS spectra obtained from $(NH_4)_2S$ and TAM treated samples after 30 minutes with air atmosphere exposed is displayed in Figure 10. Figure 10 (a) shows the complete removal of As-O bonds on both two sample surfaces. Peaks centered at 40.8eV represent As-In bonds. However, it did not show any appreciable sulfur bonds with As with a peak around 43.4eV. A possible explanation might be that the As atoms were not exposed to etch solutions long enough since the etching of the surface is not uniform. Another explanation might be that sulfur has preference to create bonds when dealing with In, Ga, As, Sb. For instance, it might be much more preferred to create In-S bonds rather than As-S bonds. Another XPS study in chapter 3.3 also supplies this hypothesis.

Figure 10 (b) illustrates the Ga spectra with the peak of 2p centered at 1117.2eV/1117.3eV corresponding to Ga-Sb bonds. An obvious Ga-S bonds can be observed at 1117.7eV with no Ga oxides left for TAM-treated sample. However, $(NH_4)_2S$-treated sample depicts gallium oxide bonds at 1118.3eV and no Ga-S bonds present.

In Figure 10 (c), XPS for In indicates presence of sulfides at 444.7eV without presence of In-O bonds for $(NH_4)_2S$-treated and TAM-treated samples. More importantly, compared to $(NH_4)_2S$ the relative strength of In-S bonds for TAM-treated sample is higher. The peak centered at 444.3eV corresponds to In bonds with As and Sb..

In Figure 10 (d), a much stronger Sb sulfur bonds at 538.8eV in TAM-treated superlattice sample is observed compared to that from $(NH_4)_2S$-treated sample. Sb-Ga bonds have the peak at 537.3eV. It is highly possible besides Sb-S bonds, In-S and Ga-S also make contributions to the peaks.

Compared to $(NH_4)_2S$, TAM solution is a highly polar molecule which can get adsorbed more robustly and promptly on a surface, resulting in a more effectiveness of the surface sulfidication for InAs/GaSb superlattice devices.

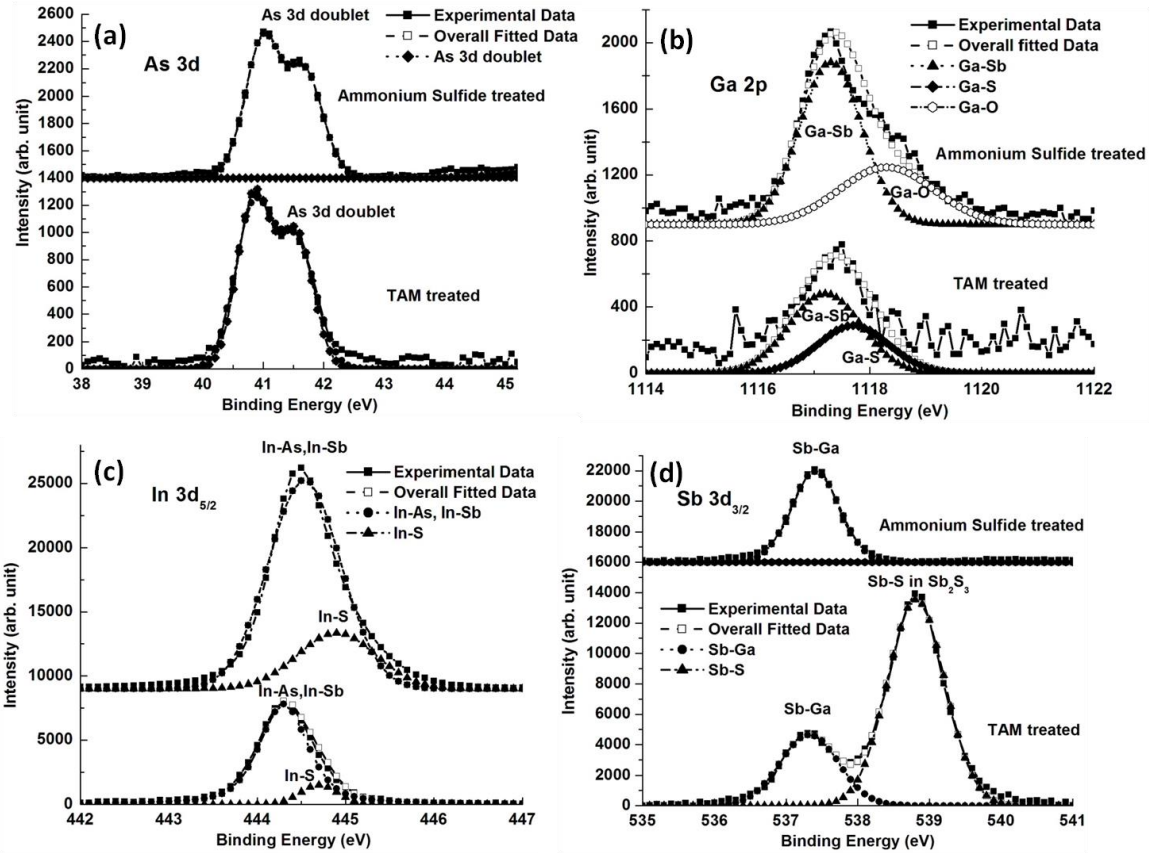

Figure 10 XPS spectra for (a) As (b) Ga (c) In and (d) Sb for (NH4)2S treated and TAM-treated samples with 30 minutes exposure

3.3 TAM-treated atomic layer deposition (ALD) 0, 1 and 2nm ZnS-Capped sample

3.3.1 Experimental Procedures

The studies were performed on InAs/GaSb type-II SLS structures consisted of 13 monolayers (ML) InAs/7 ML GaSb/1.3 ML InSb for 300 periods with the thickness of 1.86 μm. A solid source molecular beam epitaxy (MBE, VG system) are used to grow the superlattice on Te-doped n-type GaSb (100) substrate. And it was unintentionally with 4×10^{16} cm^3 n-type doped at room temperature. In order to compensate the strain in the growth direction, a thin InSb layer was incorporated in SLS repeated layers. HRXRD was used to ensure quality of the grown superlattice structure. Three small samples with a 5mm × 5mm section each were diced from the wafer that are grown from MBE system.

First, the samples were degreased in acetone and methanol, then rinsed in deionized (DI) water, blown dry with nitrogen gas. Surfaces were then etched using a hydrogen peroxide (H_2O_2), phosphoric acid (H_3PO_4), and DI water solution with a ratio of 2:1:20 etching for 30 seconds. Then, the samples were soaked in TAM solution (0.2 mol/L) with adjusted pH of 2.0 by adding acetic acid (10%) for 30 min at 70 °C. After that, one sample was left in vacuum for comparison purpose while the other two were transferred for ALD ZnS Passivation Process.

The ALD of ZnS made use of diethylzinc (DEZn) and H2S (99.5%) precursors in a tubular hot wall ALD reactor maintained at 200 °C; during deposition, both DEZn and H_2S were kept at

room temperature (25 °C). Pure Argon gas was used as the carrier gas for the delivery of each precursor and as the purge gas for system cleaning between the delivery of the precursors. In this experiment, 1nm and 2nm ZnS was deposited on the surface, respectively. The thicknesses of ZnS thin films were measured using a spectral ellipsometer.

XPS measurements were operated with a Kratos Axis-165 system equipped with Al Ka x-ray source operated at 10 mA and 15kV. The XPS measurements were done under ultrahigh vacuum with base pressure around 5×10^{-7} mtorr at room temperature with 0.1 eV step size, 300 ms dwell time. X-ray photoelectron spectra analyses were performed by element spectral peak-fitting. The binding energy are calibrated with the spectral line of C 1s at 284.6 eV. The XPS peaks were modified by Shirley-type backgrounds and Gaussian-Lorentzian peak shape functions with software XPS PEAK.

3.3.2 Results and Discussion

Figure 11 shows the XPS spectra of In 3d5/2, As 3d, and Sb 3d3/2 with 1 and 2 nm-thick and without ALD ZnS capped InAs/GaSb SLSs with TAM treatment. Binding Energies and peak intensity percentages for each element of the components were identified and quantified in Figure 11. Figure 11(a) clearly illustrates presence of In-S at SLS surface after ALD ZnS, due to a great increase in peak at 444.7 eV in middle and top graphs (TAM + 1,2 nm ALD ZnS) compared to bottom graph (TAM only). Peak centered at 444.1 eV corresponds to In 3d5/2 bonded to As/Sb. Absence of shifted peak of In3d5/2 at 445 eV shows the removal of native oxide of In by TAM

treatment. In Figure 11 (b), for only TAM-treated sample (bottom graph), spectra peak at 42.9 eV goes to As-S. However, after the ALD ZnS (middle and top graph), peaks for As-S disappear from the spectra, and this corroborates the tandem increase of the indium sulfide XPS feature. Doublets of As 3d bonded to In at 40.7 eV can be observed in all three samples which illustrates that As-In is present at the surface before and after ALD ZnS. For As-O which has a higher binding energy centered at 45.7 eV, no peaks are observed, showing the complete removal of native oxides of As. In Figure 11 (c), for TAM-treated sample (bottom graph), lower binding energy centered at 537.3 eV is assigned to In-Sb while higher binding energy at 538.8 eV is attributed to Sb-S resulting from TAM treatment. However, after ALD ZnS, Sb-S disappears at the surface with no peaks at 538.8 eV. Also, the lack of peaks at 5400 eV shows that native oxides of Sb are effectively removed with TAM treatment. Binding energy changes of Ga 2p were also analyzed in these samples, however, no peaks could be observed; this is due to low exposure of Ga to XPS system where Ga is covered by other components and could not be detected.

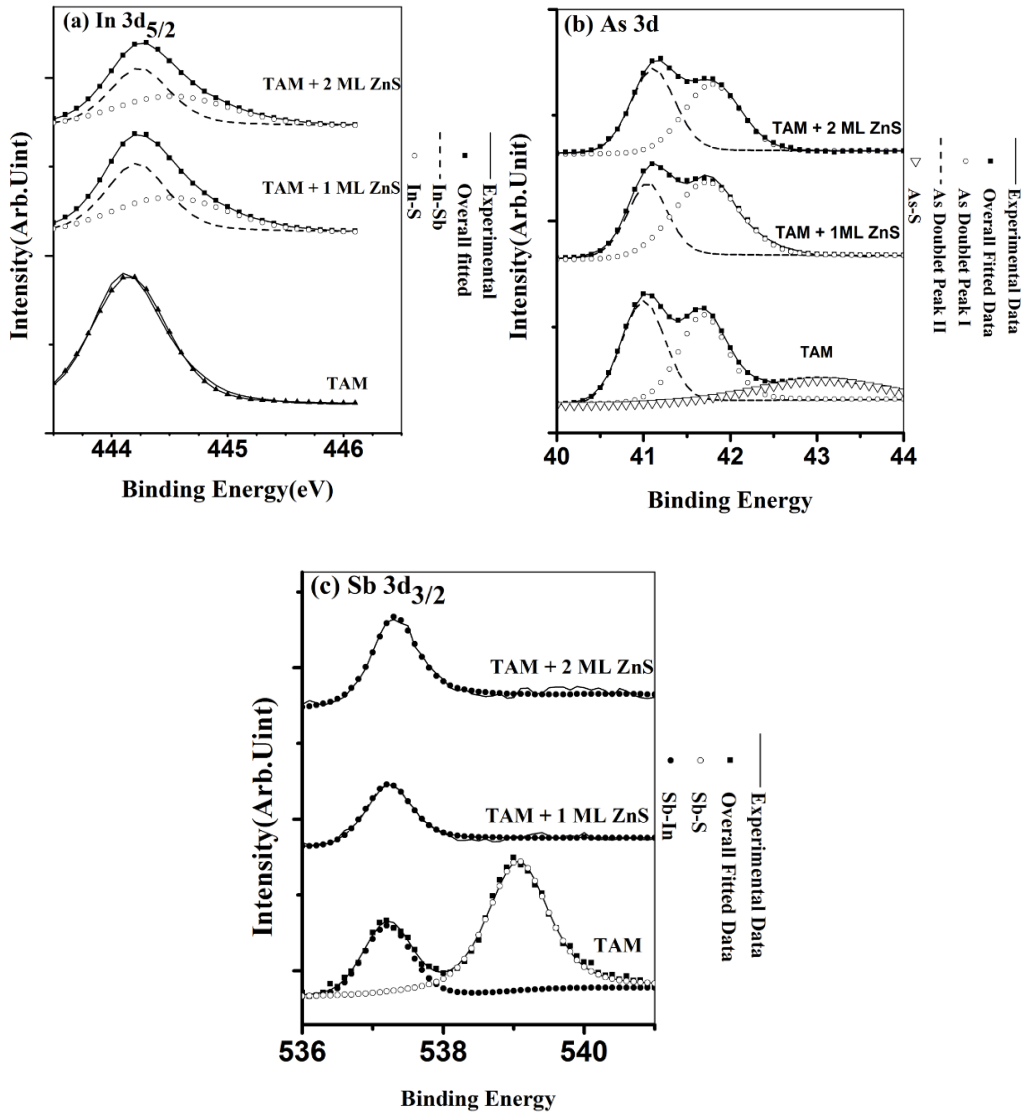

Figure 11 XPS spectra for (a) In (b) As and (c) Sb 2d3/2 for only TAM treated, TAM treated with 1nm ZnS capped, and TAM treated with 2nm ZnS capped Type II InAs/GaSb SLS samples.

Therefore, different sulfides are generated at the surface of samples only with TAM treatment. However, after ALD of ZnS, Sb–S and As–S peaks disappear while In-S peak gets enhanced which means that Indium Sulfide should be the major components at the interface. Binding Energies and peak intensity percentages for each element of the components were identified and quantified.

Table I

RESULTS OF XPS MEASUREMENTS FOR TAM TREATED ALD DEPOSITED ZNS SUPERLATTICE SAMPLES

Peak	Component	Binding Energy (eV)	Intensity Percentage (%) TAM	1nm ZnS/TAM	2nm ZnS/TAM
In $3d_{5/2}$	In-As	444.1	>95	72	68
	In-S	444.7	<5	28	32
	In-O	445.0	0	0	0
As 3d	As-In	40.7	85	100	100
	As-S	42.9	15	0	0
	As-O	45.7	0	0	0
Sb $3d_{3/2}$	Sb-In	537.3	37	100	100
	Sb-S	538.8	63	0	0
	Sb-O	540.0	0	0	0

4. SIMULATION OF PASSIVATED AVALANCHE PHOTODIOES

4.1 Simulation Platform

Silvaco ATLAS [74] is a semiconductor device simulation platform that has been widely used for device engineers to simulate the electrical characteristics of semiconductor devices. It can solve process variation problems as well as the physics modeling inside the device. The major materials it simulates include silicon, III-V, II-VI, IV-IV and polymer [76].

In this chapter, ATLAS is used to simulate current-voltage characteristics of superlattice with different passivants. Also, by comparing to the experimental current-voltage experiments, the parameters for superlattice surface mechanisms are fitted.

4.2 Physical Modeling

ATLAS has a lot of built-in physical models accounting for mobility, recombination, generation, impacting ionization and tunneling. Basic mechanism that affects the current for low bandgap photodiodes are included in this simulation.

4.2.1 Drift-diffusion Model

The drift-diffusion model is solved using equation below,

$$\vec{J}_{n,p} = q(n,p)\mu_{n,p}\vec{E} \pm qD_{n,p}\nabla n,p \quad (8)$$

where q is electronic charge, n, p electron and hole concentrations, μ mobility, E electric field, D diffusion constant and and J current density while the subscripts n and p are referenced as electron and hole components.

4.2.2 Generation-recombination Model

Generation-recombination models are separated into three models: 1)radiative recombination used for optical or band-to-band transitions, 2) Auger recombination from three-carrier recombination and 3) trap assisted Schokley-Reed-Hall (SRH) mechanism.

4.2.2.1 Band-to-band (Optical) Recombination

The band-to-band are modeled by,

$$R_{opt} = C_{opt}(np - n_i^2) \quad (9)$$

where R_{opt} is the optical recombination rate, C_{opt} radiative recombination rate constant and n_i the intrinsic carrier density.

4.2.2.2 Auger Recombination

Auger recombination involves three carriers where two carriers recombine in a band-to-band transition and give out the energy to the other carrier. The formula in equation (10) for the

recombination rate is almost the same with band-to-band recombination, by just adding the density for the third carrier, which receives the released energy,

$$R_{Auger} = A_n(pn^2 - nn_i^2) + A_p(np^2 - pn_i^2) \tag{10}$$

where R_{Auger} is the net Auger recombination rate, $A_{n,p}$ Auger recombination rate constant for electrons and holes.

4.2.2.3 Shockley-Read-Hall (SRH) recombination

Shockley-Read-Hall recombination is also named as trap-assisted recombination. When there are impurity inside the lattice, a new energy state can be created, and the electron will have probability to pass through the bands. Such energy states are called deep-level traps. The localized state can absorb differences in momentum between the carriers. And this energy can be exchanged through lattice vibration.

This two-step SRH mechanism is modeled as,

$$R_{SRH} = \frac{np - n_i^2}{\tau_n \left[n + n_i \exp\left(\frac{E_{trap}}{kT}\right)\right] + \tau_p \left[p + n_i \exp\left(\frac{-E_{trap}}{kT}\right)\right]} \tag{11}$$

where *k* is the Boltzmann constant , R_{SRH} is the Shockley-Read-Hall recombination rate, and E_{trap} is the energy difference between the trap and intrinsic Fermi level.

The trap lifetime can be modified by the Trap assisted tunneling with some enhancement factors which is described in equation (11). These factors are including phonon assisted tunneling with a trap in equation (12),

$$\gamma = \frac{\Delta E_{n,p}}{kT} \int_0^1 \exp\left(\frac{\Delta E_{n,p}}{kT} u - K_{n,p} u^{3/2}\right) du \tag{12}$$

where $\Delta E_{n,p}$ is the energy scope where tunneling can happen, and $K_{n,p}$ is defined as,

$$K_{n,p} = \frac{6\pi}{3} \frac{\sqrt{2 m_{n,p} \Delta E_{n,p}^3}}{3qhE} \tag{13}$$

where $m_{n,p}$ is the tunneling mass for electrons and holes, h is Plank's constant and E is the magnitude of the electric field.

4.2.3 Surface Recombination Mechanism

Surface and interface recombination has a significant impact on the current characteristics for low bandgap superlattice photodiodes with the sudden end of the semiconductor crystal, leaving a large quantity of active states, hence traps. Also, the surfaces or interfaces are more possibly contaminated because of the exposure during the semiconductor device fabrication procedure. Surface recombination is also included as a part of carrier lifetime in equation (14),

$$\frac{1}{\tau_{n,p}^{eff}} = \frac{1}{\tau_{n,p}^{i}} + \frac{d_i}{A_i} v_{n,p}^{s} \tag{14}$$

where subscript i is the surface simulation node i, $v_{n,p}^{s}$ is the device surface recombination velocity, $\tau_{n,p}^{i}$ is the bulk lifetime, $\tau_{n,p}^{eff}$ is the effective lifetime, d_i is the length of the interface and A_i is area of the interface. This modification of lifetime equation is only effective at the semiconductor-insulator interface.

Band-to-band tunneling is another important current mechanism in a low bandgap diode under relatively large reverse bias. Band to band tunneling generation is described in equation below,

$$G_{BBT} = \alpha E^{\gamma} exp\left(\frac{\beta}{E}\right) \tag{15}$$

where α and β are constants relating to the bandgap and the effective tunneling mass. Besides, the surface shunt effect is also included by adding a resistance which is in parallel to the device.

4.3 Device Structure and Materials

The device structure is shown in Figure 12. The device dimensions and dopings were originally kept exactly the same with the device we fabricated and characterized in the

experiments. However, during computation of n-N heterojunctions inside the device, the simulation failed to converge. Since the device operation mainly focus on P-n heterojuction not n-N heterojunction, we replaced it with an n-N homojunction to solve this computation problem.

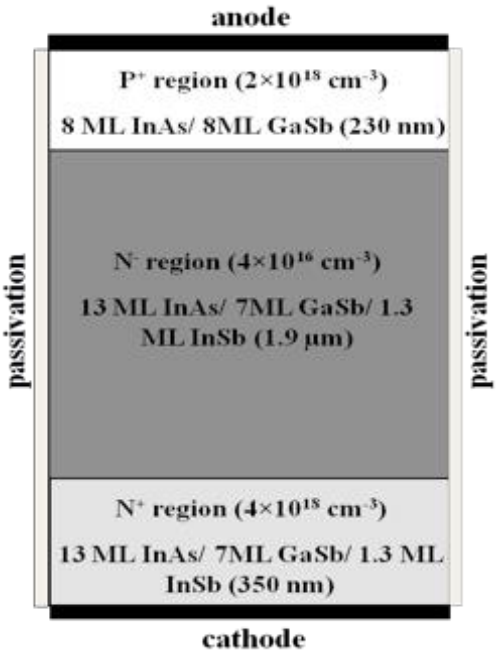

Figure 12 SLS Device Structure

In this thesis, we are investigating superlattice materials. Since superlattice is a relatively novel material, ATLAS does not include any superlattice material parameter module into its simulation. Therefore, we have to manually define the superlattice as a bulk and put the superlattice properties into this bulk. Accurate parameter values for superlattice can ensure the correctness of implementation for specified physical models above. Different designs of superlattice structure can lead to different material properties. Therefore, it is extremely difficult to generate all parameter values for overall superlattice unless it includes some theory model in it which can simulate the band structures in the superlattice.

The parameter used for the LWIR region are shown in Table II. For the structure in this simulation, the bandgap was kept the same with experimental result with cut-off wavelength of ~10 μm. Electron permittivity and affinities were computed as a mean from bulk GaSb and InAs values. The electron and hole effective mass were determined by 14 band k.p simulations. SRH lifetimes, Hole and electron mobility, radiative and Auger recombination rates were calculated or cited from existing literature [82]. The effective trap tunneling mass was calculated as an average from effective electron and hole masses. A near gap bulk trap density with 2×10^{16} cm^{-3} was included.

Surface mechanism parameters vary with different passivants. Therefore, surface properties such as surface recombination velocities, surface interface traps and shunt resistance are fitted to match the experiment results.

Table II

LWIR SLS PROPERTIES

Parameter	Values
Bandgap	0.124 eV
Permittivity	14.985
Electron affinity	4.29 eV
Electron effective mass	0.023 m_0
Hole effective mass	0.104 m_0
Electron mobility	1000 $cm^2/V\text{-}s$
Hole mobility	270 $cm^2/V\text{-}s$
SRH lifetime	90 ns
Radiative recombination rate	4×10^{-10} cm^3/s
Electron Auger recombination rate	4×10^{-26} cm^6/s
Hole Auger recombination rate	4×10^{-28} cm^6/s
Effective tunneling mass	0.0232 m_0

4.4 Simulation Results

4.4.1 Carrier concentration and electric field under equilibrium

By constructing the device structure and filling appropriate parameters into physical models, the major carrier concentrations under equilibrium are 2×10^{18} cm^{-3} for P^+, 4×10^{18} cm^{-3} for n^+ and 4×10^{16} cm^{-3} for n^- displayed in Figure 13. All of these values are identical to the values during the experiment, which indicates the correctness of the simulation. Figure 13 clearly depicts the P-n heterojunction and n-n^+ homojunction.

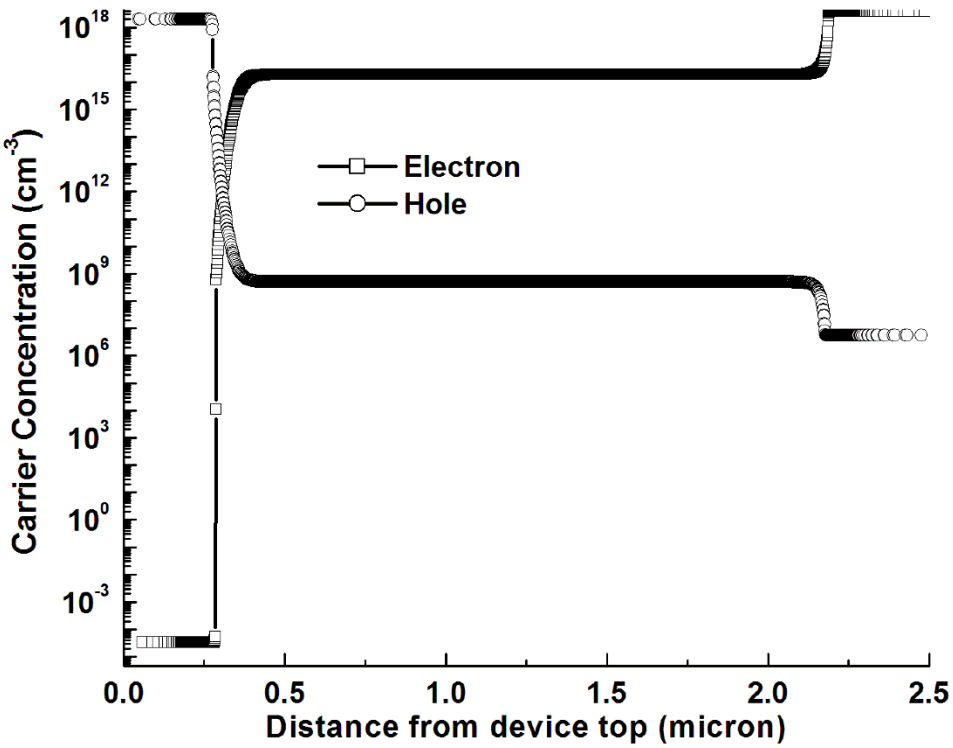

Figure 13 Simulated carrier concentrations under equilibrium

Electric field across the device under equilibrium Position are present in Figure 14. The electric field reveals triangular shapes at the heterojunction and homojunction with peak values around 3×10^4 V/cm and 4×10^4 V/cm respectively. The electric field at the N-n homojunction is slightly higher than that in the heterojunction while the depletion width is relatively thinner. Also, with the increase of reverse bias, the depletion width is expected to be wider.

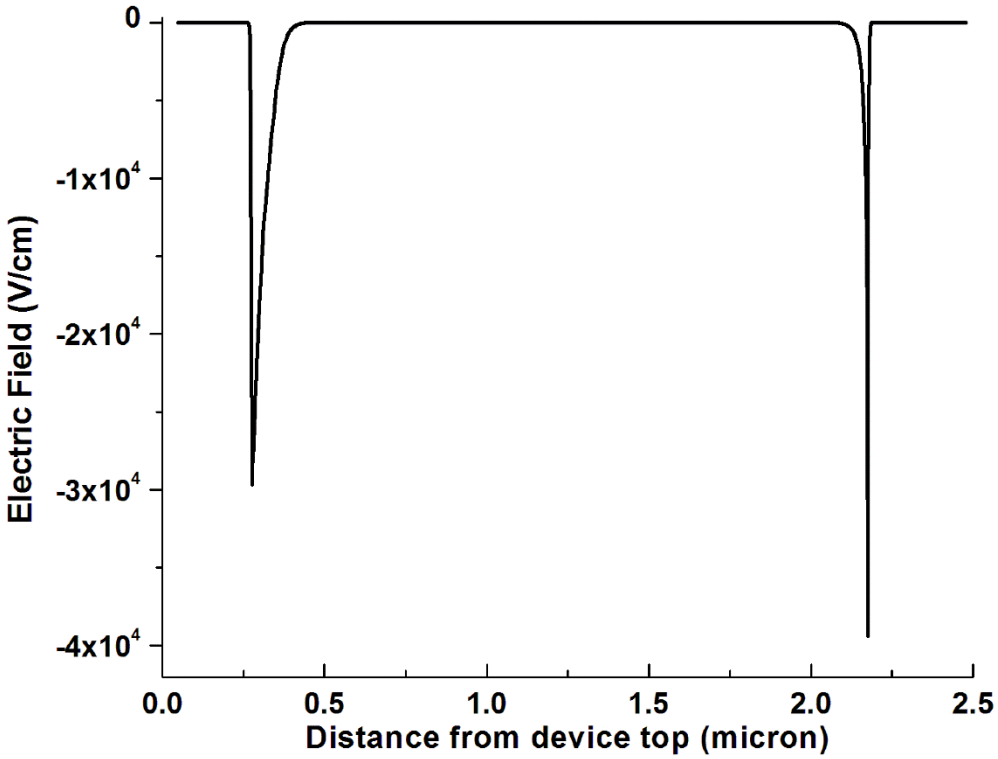

Figure 14 Simulated electric fields under equilibrium

4.4.2 Surface parameters fitting and current-voltage curve

During the first trial with parameters above, an absurd high current density occurred. After careful inspection, an unusual enormous tunneling current took place at the heterojunction. However, band to band tunneling in a heterojunction is fairly hard since it is hard for carriers to

acquire the conservation of energy and momentum with different effective mass and band structures. Therefore, the values of the constants α and β were changed to 6×10^{16} and 7×10^{5} Vcm^{-1} with higher effective tunneling masses. Meanwhile, the original effective tunneling mass was reserved for the trap-assisted tunneling.

Fitted surface parameters are characterized in Table III. Surface recombination velocities of electrons and holes for unpassivated, Si_xN_y and ZnS passivated supperlattice devices are 10^5 cm/s and 10^7 cm/s, 10^3 cm/s and 10^5 cm/s, 10^2 cm/s and 10^3 cm/s respectively while SiO_2 expects a negligible recombination velocity. For the interface trap densities, ZnS passivated devices exhibit a density of 10^{10} cm^{-2} which is the least compared to 10^{15} cm^{-2} and 8.5×10^{14} cm^{-2} for unpassivated and Si_xN_y passivated devices. Likewise, SiO_2 passivated devices have a negligible trap density compared to other three. However, shunt resistance for unpassivated and SiO_2 passivation are 0.52 Ω-cm^2 and 0.55 Ω-cm^2, which are at least one order smaller than Si_xN_y and ZnS passivated devices.

Therefore, SiO_2 passivated devices surface current are mainly affected by shunt leakage current with negligible surface recombination and traps assisted mechanism. Si_xN_y passivated devices exhibit a relatively smaller surface recombination rate and bigger shunt resistance while keeping interface trap density at the same level. ZnS passivated devices shows the improvement in all these three aspects which corresponds to the experiment result indicating a smaller current-voltage curve.

Table III

FITTED SURFACE PARAMETERS FOR DIFFERENT PASSIVANTS

Surface Passivant	**Surface Recombination Velocity (cm/s)**		**Interface Trap Density (cm^{-2})**	**Shunt Resistance (Ω-cm^2)**
	Electron	**Hole**		
Unpassivated	10^5	10^7	10^{15}	0.52
SiO_2 Passivated	-	-	-	0.56
Si_xN_y Passivated	10^3	10^5	8.5×10^{14}	55
ZnS Passivated	10^2	10^3	10^{10}	-

By fitting the surface parameters, current-voltage characteristics for the unpassivated and passivated SiO_2, Si_xN_y and ZnS devices were successfully plotted in Figure 15 which is almost identical to experiment results.

Moreover, root mean square errors for unpassivated and passivated SiO_2, Si_xN_y and ZnS devcices were calculated to be 0.0981 Acm^{-2}, 0.0382 Acm^{-2}, 0.0083 Acm^{-2} and 0.00016 Acm^{-2}.

From the simulation, surface recombination, along with shunt resistance dominate the current at a lower bias while interface trap-assisted tunneling are enhanced at higher bias.

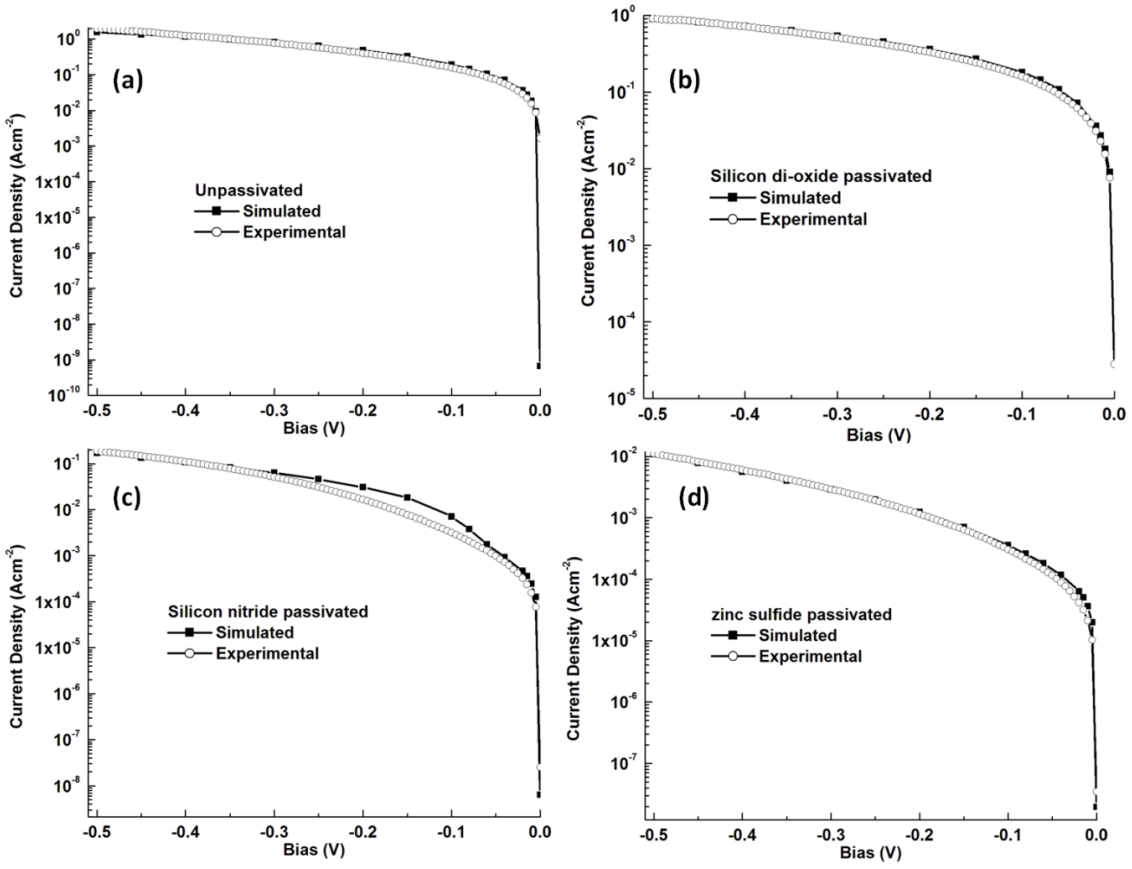

Figure 15 Current-voltage simulated for (a) unpassivated and (b) silicon dioxide (c) silicon nitride and (d) zinc sulfide passivated superlattice APDs compared with experimental results

4.5 Discussion and conclusions

4.5.1 Limitation for ATLAS

During the simulation of superlattice devices current-voltage characteristics, several ATLAS limitations are encountered. The software cannot handle superlattice materials right now. It requires us to define it as a bulk and fill in all material properties that we calculated or cited from experiments and publications. The numerical analysis of the n-N heterojunction does not converge during the iterative computations which forced us to change to a homejunction. Also, higher effective mass is manually modified due to an absurd high current density coming from the band-to-band tunneling in the n-P heterojucntion. Finally, since low bandgap photodiodes usually require low operating temperature, ATLAS lacks a robust simulation environment at low temperatures.

4.5.2 Insight of Parameter Fitting

This ATLAS simulation and parameter fitting supplies an alternative way to find out the prominent mechanism under surface leakage current for different passivation. Compared to

experimentally extracted surface recombination velocity values of ~4×10^5 cm/s [88] for ZnS passivation with $(NH_4)_2S$ treatment as a whole accounting for surface current, this simulation separates them into three different parameters (recombination velocity, trap density and shunt resistance). It might work at lower bias when recombination velocity is in effect. However, during high biases the trap-assisted tunneling can be critical that the experimental data did not account for.

Therefore, this simulation offers more details for the surface leakage current. It enable to compare the current with different passivation materials and techniques and discover the main mechanism behind the certain conditions. It also offers an insight in what aspect that we can improve the characteristics more efficiently.

5. DUAL-CARRIER AVALANCHE PHOTODIOE STRUCTURE DESIGN

In this chapter, novel avalanche photodiode structures with alternate carrier multiplication nanometer regions, placed next to a wider electron multiplication region, to create dual-carrier feedback systems, are discussed. This work was published in [99] at IEEE Transactions on Electron Devices. Gain and excess noise factor of these structures are calculated based on the dead space multiplication theory under uniform electric field. The equivalent impact ionization ratios are derived and compared. It is observed that the proposed structures can generate much higher gain compared to conventional pure electron multiplication structures under the same electric field without severely degrading the excess noise quality.

5.1 Dead Space Multiplication Theory

Carriers cannot get impact ionization without the conservation of energy or momentum. Instead, it requires a minimum distance for a new generated carrier traveling along or against the electric filed, to acquire the threshold energy. And this minimum distance the carrier traveled is called the dead space [90]. The electron and hole dead space, denoted by d_e and d_h respectively, are given by

$$d_e = \frac{E_{ie}}{q\varepsilon} \tag{16}$$

$$d_h = \frac{E_{ih}}{q\varepsilon} \tag{17}$$

where ε is the uniform electric field in the multiplication region, q is the electronic charge, E_{ie} and E_{ih} are the ionization threshold energies for the electron and hole, respectively.

For a single multiplication region with the same threshold energy, equation (16) and (17) are enough. However, when it is applied to several thin multiplication regions with different threshold energies, dead space for electrons and holes around the boundaries should be modified.

Consider a multiplication region which begins at $x = 0$ and ends at $x = W$, and the direction of the inside electric field points from the end to the front. The gain and excess noise factor have been reported in [10] under uniform electric field and then extended in [11] to non-uniform electric fields. We will review germane aspects of the model briefly. Following [10], the random gain of $Z(x)$ is expressed as the overall electrons and holes generated by a parent electron at location x. Also, $Y(x)$ is the random gain of the overall electrons and holes generated by a parent hole. Therefore, the random gain of the device can be expressed as $G = \frac{1}{2}\big(Z(0) + Y(0)\big)$. For the case of electron injection, since $Y(0) = 1$, the random gain can be simplified to $G = \frac{1}{2}(Z(0) + 1)$. According to [11, Eqs. (4) and (5)], z(x) and $y(x)$ can be obtained by

$$z(x) = \left[1 - \int_{-\infty}^{W-x} h_e(x,\xi)\, d\xi\right] + \int_{x}^{W} [2z(\xi) + y(\xi)] \cdot h_e(x, \xi - x)\, d\xi \tag{18}$$

$$y(x) = \left[1 - \int_{-\infty}^{x} h_h(x,\xi)\, d\xi\right] + + \int_{0}^{x} [2y(\xi) + z(\xi)] \cdot h_h(x, x - \xi)\, d\xi \tag{19}$$

where h_e and h_h are the probability density functions for electron and hole impact ionization. The PDFs take the following form [11, Eqs. (1a) and (1b)]

$$h_e(x,\eta) = \begin{cases} 0, & \eta < d_e(x) \\ \alpha(\eta + x) e^{-\int_{d_e(x)}^{\eta} \alpha(x+\sigma) d\sigma}, & d_e(x) \leq \eta \leq W - x \end{cases} \tag{20}$$

$$h_h(x,\eta) = \begin{cases} 0, & \eta < d_h(x) \\ \beta(x - \eta) e^{-\int_{d_h(x)}^{\eta} \beta(x-\sigma) d\sigma}, & d_h(x) \leq \eta \leq x \end{cases} \tag{21}$$

where α(y) is the ionization probability density of the electron which may ionize at location $y \in [x + d_e(x), W]$ after it travels without ionizing a distance $d_e(x)$. Similarly, β(y) is the ionization probability density of the hole that may ionize at location $y \in [0, x - d_h(x)]$after it travels in an opposite direction without ionizing a distance $d_h(x)$. Thus, the mean gain $\langle G \rangle$ can be obtained as

$$\langle G \rangle = \frac{1}{2}[z(0) + 1] \tag{22}$$

while the excess noise factor of the multiplication process, F, is given by [10, Eqs. (11)]

$$F = \frac{\langle G^2 \rangle}{\langle G \rangle^2} = \frac{z_2(0) + 2z(0) + 1}{(z(0)+1)^2} \tag{23}$$

where $z_2(x)$ is the second moment of $Z(x)$. For $0 < x < W$, it can be described as

$$\begin{aligned} z_2(x) &= \langle Z^2(x) \rangle \\ &= \left[1 - \int_{-\infty}^{W-x} h_e(x,\xi)\, d\xi\right] \\ &+ \int_0^x [2z_2(\xi) + y_2(\xi) + 4z(\xi)y(\xi) + 2z^2(\xi)] \cdot h_e(x, \xi - x) d\xi \end{aligned} \tag{24}$$

and $y_2(x)$ is the second moment of $Y(x)$, determined as

$$\begin{aligned} y_2(x) &= \langle Y^2(x) \rangle \\ &= \left[1 - \int_{-\infty}^{W-x} h_h(x,\xi)\, d\xi\right] \\ &+ \int_0^x [2y_2(\xi) + z_2(\xi) + 4z(\xi)y(\xi) + 2y^2(\xi)] \cdot h_h(x, \xi - x) d\xi \end{aligned} \tag{25}$$

while at $x = W$,

$$z_2(W) = 1 \tag{26}$$

and at $x = 0$,

$$y_2(W) = 1 \tag{27}$$

The expected gain and excess noise factor can be estimated by solving the recurrence equations (18), (19), (24) and (25) using iterative numerical method.

5.2 Novel Structures and application of dead space multiplication theory

An APD with conventional separate absorption and multiplication (SAM) [95] structure is shown in Figure 16(a). In order to show the structure, area "Absorption" denotes SLS structure region for absorber, "Electron Multiplication" for electron multiplication region.

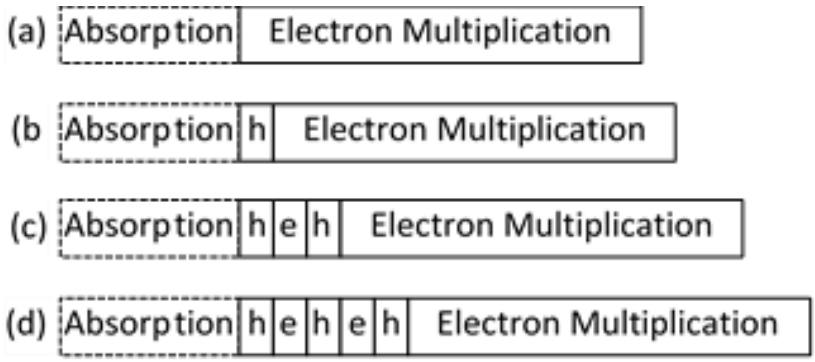

Figure 16 Four different multiplication structures: (a) single carrier (electron) multiplication, (b), (c), (d) dual carrier multiplication

The proposed device structure is shown in Figure 16 (b) which also contains the absorber and electron multiplication region. A thin hole multiplication region noted by “h” is inserted between absorber and electron multiplication regions in this device structure. Electron and hole multiplication regions were implemented using type-II SLS materials used previously in electron- [91] and hole- [92] APDs. The design implemented with above materials ensures that only electrons initiate the avalanching process in the electron-multiplication region and holes in the hole-multiplication region.

We assume that the electric field extends from area “Electron Multiplication” to area “Absorption” in both structures (a) and (b). In structure (a), electron-hole pairs are created from electron impact ionizations. Secondary electrons may also get impact ionized as long as they travel farther than their dead-space distance, acquiring energy more than ionization threshold energy. However, the secondary holes will leave the multiplication region without any impact ionization since the material in this region is band-structure engineered to have pure electron multiplication. Nonetheless, in structure (b), when the secondary holes travel through the thin hole multiplication region “h”, they also have the possibility to impact ionize since this region is designed for hole multiplication. Thus, extra electron-hole pairs are created compared to structure (a). Furthermore, the secondary electrons created in region “h”, that are drifted into electron multiplication region by electric field, can also impact ionize. This results in additional electron-hole pairs and also allows newly created holes to impact ionize again in region “h”. Therefore, a dual-carrier feedback

system is created and higher gain can be expected since many more electron-and-hole pairs are generated. For structures in Figure 16 (c) and (d), with more thin layers alternatively added, larger gain can be expected not only because the hole impact ionization possibility increases, but also more feedback paths are created.

In order to simulate gain and excess noise, it is necessary to determine dead spaces (d_e and d_h) for electrons and holes. For a certain uniform electric field, the ionization threshold energies were assumed to be equal to their bandgaps and ionization coefficients were extracted from experimental gain variation with bias from [91].

However, when two or more thin multiplication regions are present, dead spaces for carriers within a distance less than dead space to the boundaries between two thin multiplication regions should be modified.

For example, if one electron is generated at a position (x=x') with a distance ξ' to the boundary (x=b), and under electric field it drifts toward the boundary. If ξ' is large enough, it can get impact ionized after it travels a dead space distance in this region. And the dead space $d_e(x')$ is described as $d_e(x') = d_{e1} = \frac{E_{ie1}}{q\varepsilon}$, where q is the electronic charge, ε is the uniform electric field, E_{ie1} are the ionization threshold energy of the electron in its original multiplication region.

However, if ξ' is less than its dead space d_{e1}, the electron will reach the boundary without ionization. Thus, when this electron enters into the second region, it carries a kinetic energy, $E_e'=q\varepsilon\xi'$, which describes the energy this electron accumulates under electric field ε drifting with a distance ξ'. If E_e' is larger than the threshold energy E_{ie2} for electron in the second region, the electron will impact ionize immediately. If it is smaller, the electron still has to travel with a distance to achieve the threshold energy for electrons in the second region. Therefore, under the condition of $\xi' < d_{e1}$, the dead space of this electron can be modified as

$$d_e(x') = \begin{cases} \xi', & E_e' \geq E_{ie2} \\ \xi' + \dfrac{E_{ie2} - E_e'}{q\varepsilon}, & E_e' < E_{ie2} \end{cases} \tag{28}$$

Where q is the electronic charge, ε is the uniform electric field, E_{ie2} are the ionization threshold energy of the electron in the second multiplication region. E_e' is the initial energy of electron when it enters into the second regions.

Similarly, for a hole generated at a position ($x=x'$) with a distance ξ'' to the boundary ($x=c$) where ξ'' is less than dead space d_{h1} and under electric field it drifts to the boundary, in its original region, the dead space can be modified as

$$d_h(x') = \begin{cases} \xi'', & E_h' \geq E_{ih2} \\ \xi'' + \dfrac{E_{ih2} - E_h'}{q\varepsilon}, & E_h' < E_{ih2} \end{cases} \tag{29}$$

where q is the electronic charge, ε is the uniform electric field , E_{ih2} are the ionization threshold energies of the electron in second multiplication region. E_h' is the initial energy of hole when it enters into the second regions.

Now according to the dead-space multiplication theory, the excess noise factor is a function of the ionization coefficient ratio and the mean gain, as well as the multiplication-region width. The thickness of thin hole-multiplication region "h" is set to be thinner than the hole's dead space distance. This restriction in the multiplication width ensures that only those carriers that gain sufficient energy prior to entering the thin region can impact ionize. The structure does not provide enough distance for secondary carriers to build up their energy to the threshold-energy level. This reduces the randomness of ionization (position randomness) for holes, so as to minimize the excess noise factor. Dead spaces calculated for holes in hole multiplication region and electrons in electron multiplication region are around 170 nm and 107 nm, respectively at an electric field of 20 kV/cm. Thus, thicknesses are 10 nm which is almost one tenth of its dead space for thin hole multiplication region "h", 10 nm for thin electron multiplication region "e" and 800 nm for wide electron multiplication region "Electron Multiplication".

5.3 Modeling Results and Discussion

Variations of the mean gain with applied electric field for the different structures are illustrated in Figure 17. The results highlight the increase of multiplication gain through higher carrier feedback generated in additional thin multiplication regions. To be more specific, in order to achieve a gain of 40, only a bias of 2.1 V needs to be applied to structure (d) instead of 17.6 volts to structure (a). Thus, the required bias is reduced by almost 8 times at this gain. As previously stated, high bias can increase dark currents, especially for long wave infrared devices. Thus these new structures (from structure (b) to (d)) have a positive effect on dark current reduction. Also, they can be potentially used for low-bias high-gain applications such as single photon counting devices which can be directly integrated to Si readout circuits which operate at a relatively low voltage.

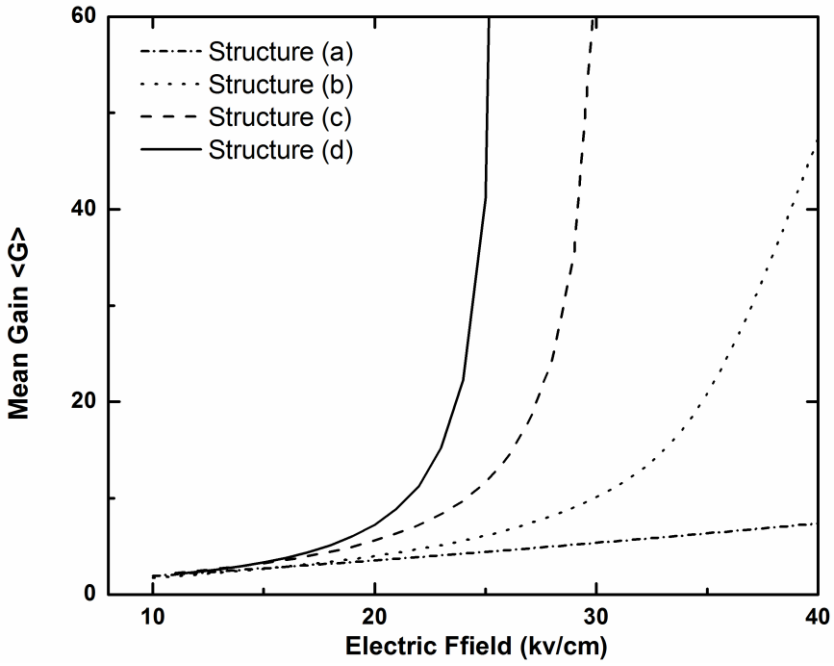

Figure 17 Comparison of different mean gain <G> with the variation of electric field across four structures (a) – (d).

From a different perspective, the additional gain from the thin multiplication layers can be traded for a lower thickness of the wider electron multiplication region. In order to study the effectiveness on the thickness reduction, thickness of the whole multiplication versus gain was quantified in Figure 18. It is shown that under an electric field of 20 kV/cm, with only adding five

thin 10 nm alternate carrier multiplication layers from structure (a) to (d), the thickness can be reduced from 1840 nm to 1009 nm at a mean gain of 20, which enables us to fabricate APD devices with smaller size.

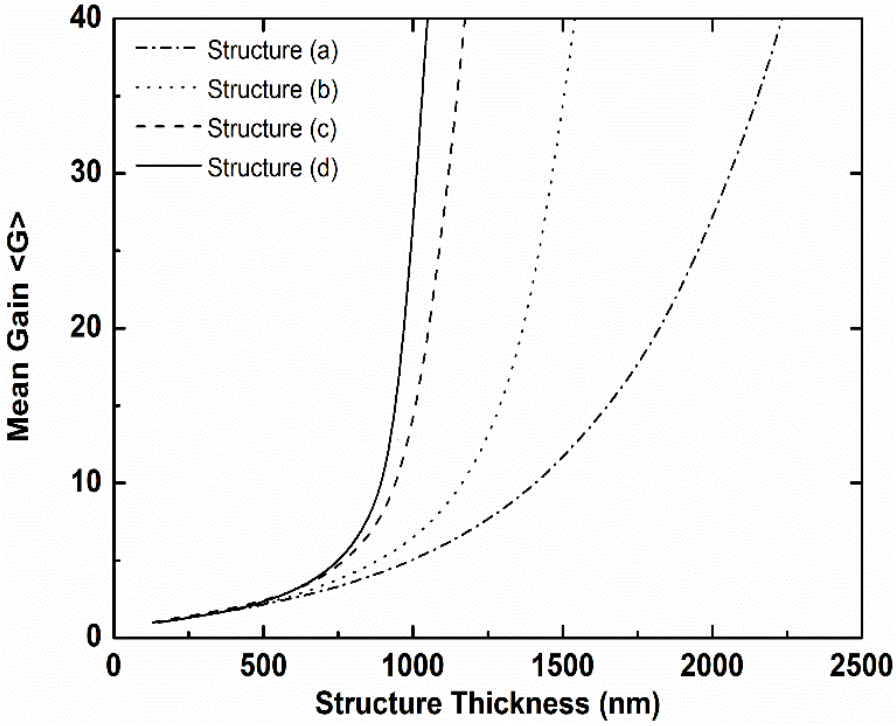

Figure 18 Comparison of the DSMT-simulated structure thicknesses as a function of mean gain <G> for all four structures.

Variations of excess noise factors versus mean gain for the different structures are displayed in Figure 19. Structure (a) which comprises of a single almost pure electron multiplication region has the least excess noise as expected from McIntyre model. It is clearly seen from the slopes of four curves that the increase in excess noise with gain is progressively steeper from structure (a) to structure (d).

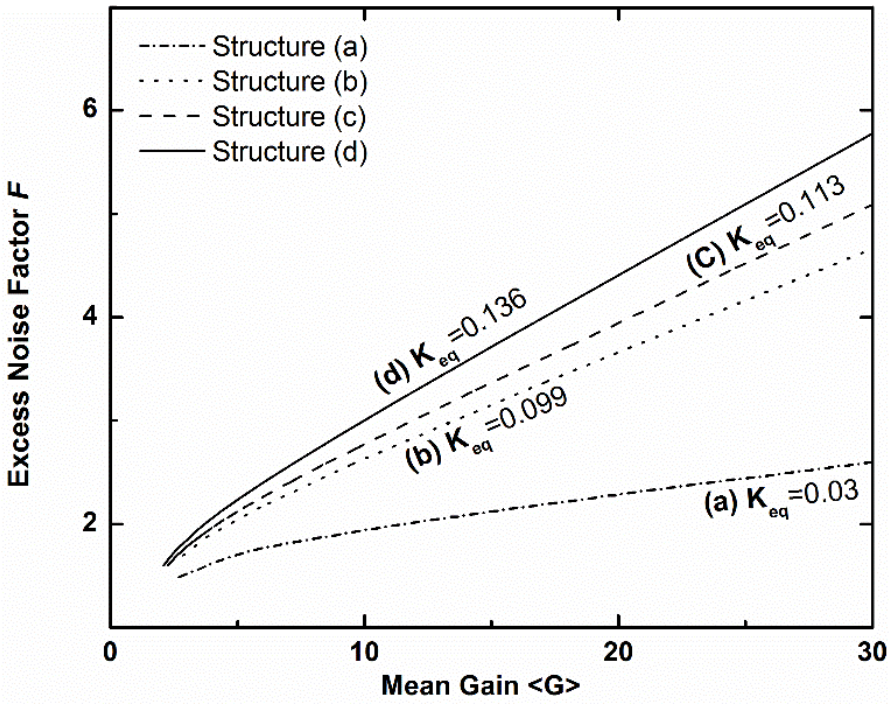

Figure 19 Comparison of the DSMT-computed excess noise factors F for structures (a), (b), (c) and (d) as a function of mean gain <G>

To better understand and control the excess noise factor in the proposed dual-carrier APD structure, the overall equivalent impact ionization coefficient ratio k_{equiv} has been calculated with variable thickness of the thin carrier multiplication region in Figure 20. k_{equiv} can be determined by using the conventional expression for the excess noise factor as

$$F = k\langle G\rangle + (1-k)\left(2 - \frac{1}{\langle G\rangle}\right) \tag{30}$$

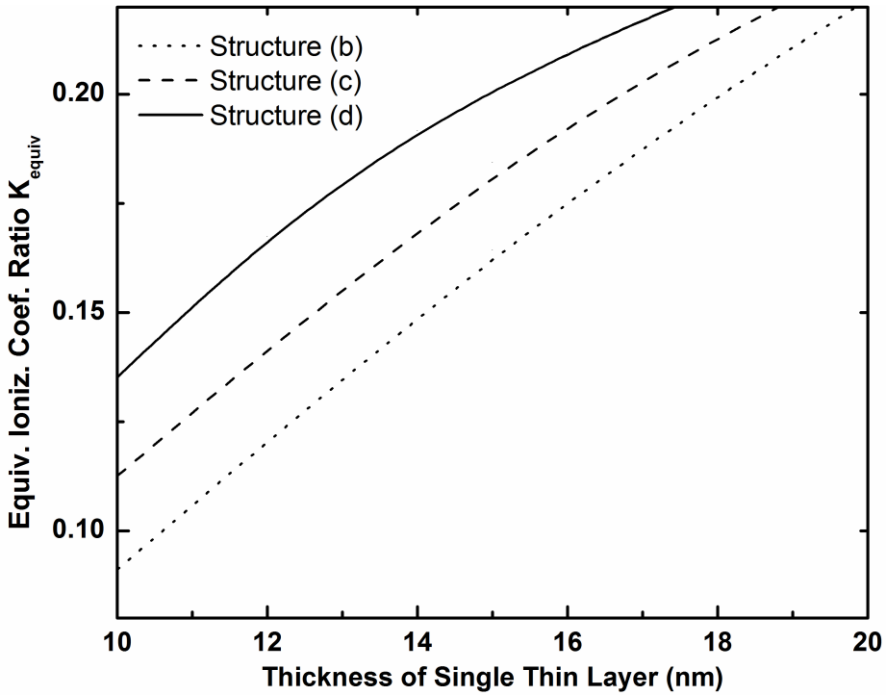

Figure 20 Comparison of the DSMT-simulated equivalent ionization coefficient ratios k_equiv for structures (b), (c) and (d) as a function of thickness of single thin multiplication region layer

Hence, if the overall mean gain $\langle G \rangle$ and excess noise factor F are known, Keq can be calculated as

$$k_{equiv} = \frac{F - \left(2 - \frac{1}{\langle G \rangle}\right)}{\langle G \rangle + \frac{1}{\langle G \rangle} - 2} \tag{31}$$

Simulations are performed under a 20 kV/cm electric field with the multiplication regions having a dead space of 107 nm and 170 nm for hole and electron. By keeping the total width the same, the width of thin region is varied. It is known that the impact ionization coefficient ratio is 0.03 [91] in structure (a) since it only has electron multiplication region. In Figure 20, k_{equiv} of the different structures are compared with variable thin region width. For a thickness of 10 nm structures (b), (c) and (d) have k_{equiv} of 0.099, 0.113 and 0.136, respectively, which are higher compared to structure (a). Also, for each structure in Figure 20, k_{equiv} increases with thickness of each thin multiplication region, which is in accord with the design rule of this dual APD structure that thinner hole multiplication region decreases position randomness of impact ionization, therefore, reducing the excess noise. Thus in order to get a lower excess noise, thickness of thin multiplication regions must be minimized. However, gain decreases with that thickness as well. Therefore, there is a trade-off between gain and excess noise. Specific region thickness and materials used for this model can be selected to satisfy specific design requirements.

Finally, since only heated holes from the wider electron multiplication region impact ionize inside the thin multiplication region and the secondary carriers generated inside do not. The role of carrier heating in avalanche multiplication (also termed the "initial-energy effect") was reported

in [93] in the context of a very low-noise GaAs-based APD developed by Campbell *et al*. (referred to as Device-II in [93]). Therefore, providing the hole ionization rates unchanged for the thin h-multiplication region, the overall excess noise factors will not be affected no matter what the electron impact ionization rate is in that thin h-multiplication region. This is confirmed by simulation results shown in Figure 21.

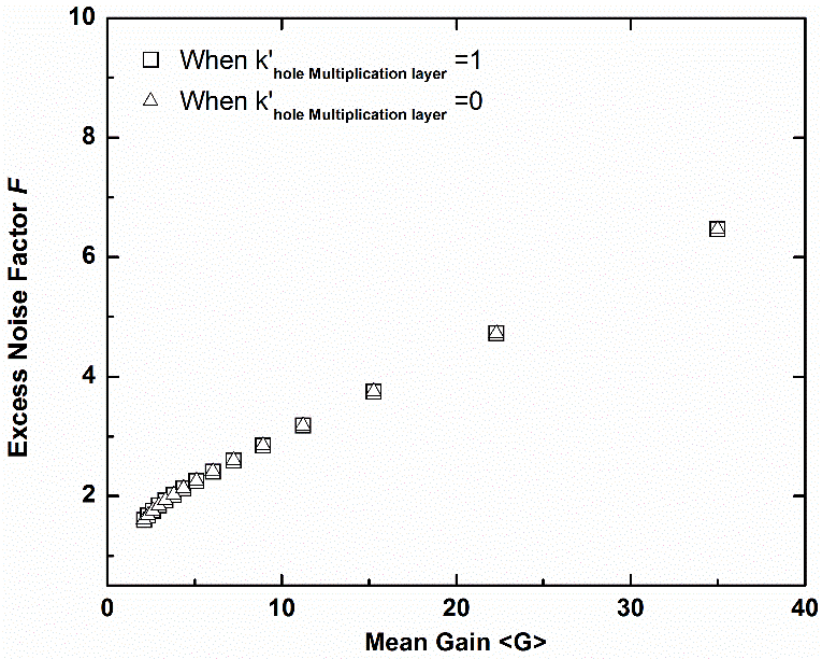

Figure 21 Variation of excess noise factor F with mean gain <G> for structure (d) when impact ionization ratio (k') in thin hole multiplication region ("h") are changed to either 0 or 1.

In Figure 21, the excess noise factor versus mean gain in structure (d) was simulated by changing the impact ionization coefficient ratio (k'=0 and k'=1) in the thin hole multiplication region while keeping hole impact ionization rate in that region the same. For different k', the same excess noise factor was achieved at the same gain. This observation provides greater flexibility in making a suitable choice, as only the value of hole ionization coefficient needs to be considered without regarding the same for electron ionization inside the thin region.

5.4 Conclusion

Novel dual-carrier feedback APD structures are designed and modeled. Different from normal SAM structures with only one multiplication region, these structures use one or multiple thin alternate hole multiplication layers placed adjacent to a wide electron multiplication region. This creates dual carrier feedback through controlled carrier multiplication inside thin layers. A specifically lattice engineered type-II SLS was used as the electron multiplication region while the thin hole multiplication region was composed of InxGa1-xSb. Simulations were carried out to predict the performance using the dead space multiplication theory.

The device design allows the APDs to have higher gains in exchange of a controlled trade-off with excess noise. Gains much higher than a single carrier APS, were achieved under a relatively low bias (<5 V), which creates the possibility of integrating dual APDs directly to silicon

read-out circuits without the need of high voltage supplies. Also, with low electric field, it can reduce dark currents in linear and dark count and after-pulsing in single photon counting applications. The width of the thin region was shown to be the most critical parameter determining the device performance. With that width increasing, both gain and excess noise increase. For its frequency response, since this APD structure includes both electrons and holes to create feedback systems, there will be a reduction in bandwidth, thus resulting in low gain-bandwidth products.

It is emphasized that these structures are novel SAM structures which combine both the hole and electron multiplication regions in different physical locations which create new gain-and-excess-noise characteristics. Although the current discussion involved only mid wavelength infrared APDs based on III-V SLS, it can be extended to other material systems where two different regions can be grown together with different carriers dominating the avalanching process. Material properties such as bandgap, ionization coefficients, band alignments need careful selection to satisfy specific application requirements

6. CONCLUSION AND FUTURE WORK

In this thesis, the simulation, fabrication and characterization of type II III-Vsuperlattice avalanche photodiode are discussed.

In the first chapter, the fundamental theories behind the photodiodes and avalanche photodiodes were introduced. Avalanche photodiodes fabricated with different materials like Si, HgCdTe and superlattice are compared. III-V Superlattice APDs presented very promising properties. First, superlattices with different thickness of layers enables the modification of band structure, not only making it possible that the structure can be tuned with the requirement of different wavelength detections, but also improving the detection quality by having larger carrier mass creating less tunneling current. Second, III-V superlattices can be grown uniformly on a relatively large areas, and they have standard fabrication procedures. It also discussed the basic material stricture design and device software engineering which will be valuable for the novel superlattice photodiode structure design in chapter 5 and photodiodes mechanism and parameters fitting in chapter 4.

Simple fabrication process of III-V superlattice photodiodes are presented in chapter 2. With the help of superlattice band structure design on III-V, electron and hole avalanche photodiodes with low excess noise are made possible. III-V superlattices that were used in this research are grown with MBE, then diced into smaller pieces with different diameters for

characteristics comparison. After that, it was patterned with photo lithography and etched by specified etch solution with a combination of deionized (DI) water, hydrogen peroxide (H_2O_2) and phosphoric acid (H_3PO_4). Finally, the metal pads are deposited with E-beam evaporation. Since MWIR and LWIR photodiodes with low band gaps are fabricated, extra step of passivation for superlattice interface and surface are accomplished in chapter 4.

Surface passivation is actively investigated recent years, either with different recipes for surface treatment such as sulfidization or different encapsulation materials (SiO_2, ZnS, etc). Surface passivation not only supplies as an insulation with outer atmosphere, but also eliminates the active states in the surface, resulting in an improvement of leakage current and breakdown voltage. Firstly, TAM- and $(NH_4)_2S$- treated superlattice surfaces are investigated with XPS. With the analysis of XPS results, a better sufidization can be achieved by TAM method, which proves that TAM treated superlattice photodiodes have a relatively low dark current compared to that of $(NH_4)_2S$ treated. Secondly, a deeper investigation of TAM- treated superlattice with different atomic layer deposited ZnS are carried out by XPS. The purpose is to find out the inner mechanism behind ZnS encapsulation for III-V superlattice. Through comparison, Sb–S and As–S peaks disappear while In-S peak gets enhanced with the deposition of ZnS, indicating that Indium Sulfide should be the major components at the interface.

Simualtions of type II superlattice APDs with different passivants were performed in chapter 4. Semiconductor device simulation software ATLAS platform is used for the simulation. Several fundamental mechanism for semiconductor device were calibrated. Also, since the software cannot simulate the properties of superlattice structures, the superlattice were seen as a bulk with its material properties filled into this bulk. The parameters are calculated or cited from the literatures or experiments. Convergence failed during the simulation at the first try, hence a heterojunction were replaced by a homejunction for n-N since this junction will not contribute a lot to the current-voltage performance. Three separate mechanism are counted for surface current: surface recombination, trap density and shunt resistance. During the fitting, another issue associated with the software numerical computation is that the band-to-band tunneling current in n-P heterojunction had a huge increase which does not make sense in practical. Therefore, the effective mass for the band-to-band tunneling is modified to match the experimental results. With all surface parameters fitted and structure built, final simulation results are almost identical to experimental result. From the simulation, surface recombination velocity and shunt leakage resistance dominate the current at lower biases while interface trap-assisted tunneling are enhanced at higher bias. By reversely analyzing the surface parameters, the surface current mechanisms were found for different passivants. SiO_2 passivated surface current are mainly affected by shunt leakage current with negligible surface recombination and traps assisted mechanism. Si_xN_y passivated exhibit a relatively smaller surface recombination velocity and shunt leakage while keeping

interface trap density at the same level with unpassivated surface. ZnS passivated devices shows the improvement in all these three aspects.

In the fifth chapter, several novel superlattice APD structure designed are proposed and simulated. The dead space multiplication theory were reviewed for SAM structures by modifying its impact ionization probability density function with an added dead space which ensures the carrier to achieve the threshold energy to get impact-ionized. Then, several new structures were designed with electron and hole avalanche materials. The main interest for this design is that it can create feedback systems for carrier impact ionizations, indicating a much larger gain compared to conventional structure while keeping the excess noise at similar level with the benefit of electron and hole APD structures. By simulating its gain, excess noise factor with different thickness layer, it is confirmed the effectiveness of this design. With the creation of more feedback layer, gain is amplified massively. It makes the design tunable between device gain and excess noise. With some applications such as single photon detector which requires a relatively high gain under the certain excess noise level, this design may be a good candidate. Certainly, a shortcoming of this structure is that with more and more feedback routes inside the device, the response time will become longer and longer. Finally, the concept of dual-carrier APDs, with carrier feedback to generate high gain and control of excess noise through confining impact ionization in thin layers, is general and can also be applied to other wavelength avalanche photodiodes with different materials and thickness.

Type II InAs/GaSb Strain Layer Superlattice allows for versatile bandstructure design leading to impact ionization coefficient engineering.

There are several improvements that can be done in the future work. First, more uniform deposition of encapsulation layer can be investigated since it will greatly reduce the active states in the surface. Second, in the novel design structure, gain and excess noise factor are already simulated with different thickness, response time is expected to increase. It can be simulated and quantified in the future. Third, with more and more new materials for electron and hole avalanche APDs coming out, the effectiveness of the novel structure can be tested. Fourth, ATLAS simulation of superlattice devices with different passivants can also be used as a tool to compare different surface current mechanisms when a new passivant coming out.

CITED LITERATURE

[1] W. Wien, *Philosophical Magazin*, Series 5, vol. 43, p. 214, 1897.

[2] U.A. Bakshi and A.P. Godes, *Basic Electronics Engineering*, p. 8, 2009

[3] G.E. Stillman and C.M. Wolfe, *Semiconductors and semimetals*, vol. 12, p. 291, 1977

[4] F. Capasso, *Semiconductors and semometals*, vol. 22, p. 1, 1985

[5] K.G. Mckay, *Phys. Rev.*, vol. 94, p. 877, 1954

[6] R. J. McIntyre, *IEEE Trans. Electron Devices*, vol. ED-13, p. 164, 1966.

[7] K. A. Anselm, P. Yuan, C. Hu, C. Lenox, H. Nie, G. Kinsey, J. C. Campbell, and B. G. Streetman, *Appl. Phys. Lett.*, vol. 69, p. 3734, 1996.

[8] J.S. Marsland, *J. Appl. Phys.*, vol. 67, p 1929, 1990

[9] B. E. A. Saleh, M. M. Hayat, and M. C. Teich, *IEEE Trans. Electron Devices*, vol. 37, p. 1976, 1990.

[10] M. M. Hayat, B. E. A. Saleh, and M. C. Teich, *IEEE Trans. Electron Devices*, vol. 39, p. 546, 1992.

[11] M. M. Hayat, W. L. Sargeant, and B. E. A. Saleh, *IEEE J.Quantum Electron.*, vol. 28, p. 1360, 1992.

CITED LITERATURE (continued)

[12] M. A. Saleh, M. M. Hayat, B. E. A. Saleh and M. C. Teich, *IEEE Trans. On Elec. Devices*, vol. 47, p. 625, 2000.

[13] P.P. Webb, R.J. McIntyre and J. Conradi, *RCA. Rev.*, vol. 27, p. 234, 1974

[14] H. Dautet, P. Deschamps, B. Dion, A.D. MacGregor, D. MacSween, R.J. McIntyre, C. Trottier, and P.P. Webb, *App. Opt.,. vol.* 32(21), p. 3894, 1993

[15] S. Vasile, P. Gothoskar, R. Farrell, D. Sdrulla, *IEEE Trans. Nuclear Science*, vol. 45, p. 720, 1998.

[16] A. Rochas, A.R. Pauchard, P.-A. Besse, D. Pantic, Z. Prijic, and R.S. Popovic, *IEEE Trans. Electron Devices*, vol. 49, p. 387, 2002

[17] M.-H. Chung, Y.-I. Choi, and S.-K. Chung, *IEEE Electron. Lett.*, vol. 26, p. 1946, 1990.

[18] Y.K.Su, C.Y.Chang, and T.S.Wu, *Opt. Quant. Electron.*, vol. 11, p. 109, 1979.

[19] K.Taira, Y.Fukuchi,R.Ohta, K.Katoh, and K.Kikuchi, *IEEE Electron. Lett.*, vol. 38, p. 1465, 2002.

[20] T.Miyata, T.Iwata, and T.Araki, *Meas. Sci. Technol.*, vol. 16, p. 2453, 2005.

[21] H. Melchior and W.T. Lynch, *IEEE Trans. Electron Devices*, vol. 13, p. 829, 1966

CITED LITERATURE (continued)

[22] S.B. Samavedam, M.T. Currie, T.A. Langdo and E.A. Fitzgerald, *App. Phys. Lett*., vol. 73, p. 2125, 1998

[23] G. Dehlinger, S.J. Koester, J.D. Schaub, J.O. Chu, Q.C. Ouyang and A. Grill, *IEEE Photonics. Tech. Lett.*, vol. 16, p. 2547, 2004

[24] Y.Liu, S.R.Forrest, J. Haldky, M.J.Lange, G.H.Olsen, and D.E.Ackley, *IEEE J. Lightwave Tech.*, vol. 10, p. 182, 1992.

[25] C.L.F Ma, M.J.Deen, and L.E.Tar, *IEEE J. Quantum Elect.*, vol. 31 , p. 2078, 1995.

[26] S.Hanatani, H.Kitano, M.Shishikura, and S.Tanaka, *Opt. Quant. Electron.*, vol. 28, p. 575, 1996.

[27] J.X.Luu and L.A.Jiang, *Appl. Optics*, vol. 45, p. 3798, 2006.

[28] Y. Zhao and S.He, *Opt. Commun.*, vol. 265, p. 476, 2006.

[29] W.G.Lawson, S. Nielsen, E.H.Putley, and A.S.Young, *J. Phys. Chem. Solids*, vol. 9, p. 325, 1959.

[30] P. Norton, *Optoelectronics Rev.*, vol. 3, p. 159, 2002

[31] J. Beck, C. Wan, M. Kinch, J. Robinson P. Mitra, R. Scritchfield, F.Ma and J.Campbell, *J. Elec. Mat.*, vol. 35, p. 1166, 2006.

CITED LITERATURE (continued)

[32] G. Perrais, O. Gravrand, J. Baylet, G. Destefanis, and J. Rothman, *J. Elec. Mat.*, vol. 36, p. 963, 2007.

[33] G. Destefanis and P. Tribolet, *Proc. SPIE*, vol. 6542, p. 723467, 2007.

[34] J.D.Beck, CF. Wan, M.Kinch, and J.Robinson, *Proc. SPIE*, vol. 188, p. 4454, 2001.

[35] M.D.Blue, *Phys. Rev.*, vol. 134, p. A226, 1964.

[36] M.A.Kinch, J.D.Beck, C-F Wan, F.Ma, and J. Campbell, *J. Electron. Mat.*, vol. 33, p. 630, 2004.

[37] A Rogalski, A Jozwikowska, K Jozwikowski and J Rutkowski, *Semicond. Sci. Technol.*, vol. 8, p. S289, 1993.

[38] P. Madejczyk, A. Piotrowski, K. Kłos, W. Gawron and J. Rutkowski, J. Pitrowski, and A.Rogalski, *Opto-Electron. Rev.*, vol. 13, p. 239, 2005.

[39] P. Becla, *J. Cryst. Growth*, vol. 121, p. 394, 1992.

[40] J. Chu and A. Sher, *Device Physics of Narrow Gap Semiconductors*.: Springer, 2010.

[41] W. Guang-Yu and P. Rui-Wu D.Yong-Qing, *J. Electron. Mat.*, vol. 23, p. 221, 1994.

[42] M. Liu, B.Y. Man, X.C. Lin, X.Y. Li, C.S. Chen, *Appl. Sur. Sci.*, vol. 253, p. 9291, 2007.

CITED LITERATURE (continued)

[43] P. Capper, *Bulk Crystal Growth of Electronic, Optical and Optoelectronic Materials*.: John Wiley and Sons. Ltd., 2005.

[44] G.C.Osbourn, *J. Vac. Sci. Technol.*, vol. B2, p. 176, 1984.

[45] D. Partin, *IEEE J. Quant. Electron.*, vol. 24.8, p. 1716, 1988.

[46] Z. Shi,M. Tacke, A. Lambrecht and H. Böttner, *App. phy. lett.*, vol. 66, p. 2537, 1995.

[47] A. Rogalski, *Infrared Detectors*.: CRC Press, 2010.

[48] S.D. Gunapala and S.V. Bandara, *Semiconductors and Semimetals*, vol. 62, p. 197, 1999.

[49] B.F. Levine, *Journ. of Appl. Phys.*, vol. 74, p. 1, 1993.

[50] H.Schneider and H.C.Liu, *Quantum Well Infrared Photodetectors: Physics and Applications*.: Springer, 2007.

[51] K.K.Choi, *The Physics of Quantum Well Infrared Photodetectors*.: World Scientific Publishing Company, 1997.

[52] J.T. Longo, D.T. Cheung, A.M. Andrews,C.C. Wang, and J.M. Tracy, *IEEE T Electron. Dev.*, vol. 25, p. 213, 1978.

[53] W. Monch, *Semiconductor Surfaces and Interfaces*, :Springer, p 54-60,1995.

CITED LITERATURE (continued)

[54] A. Gin, Y. Wei, J. Bae, A. Hood, J. Nah and M. Razeghi, *Thin Solid Films*, vol. 489, p. 447, 2004.

[55] H.S. Kim, E. Plis, A. Khoshakhlagh, S. Myers, N. Gautam, Y. D. Sharma, L. R. Dawson, S. Krishna, S. J. Lee, and S. K. Noh., *Appl. Phys. Lett., vol.* 96, p. 502, 2010.

[56] A. Hood, P. Y. Delaunay, D. Hoffman, B. M. Nguyen, Y. Wei, M. Razeghi and V. Nathan, *Appl. Phys. Lett.*, vol. 90, p. 233513, 2007.

[57] A. Gin, Y. Wei, A. Hood, A. Bajowala, V.Yazdanpanah, M. Razeghi and M. Tidrow, *Appl. Phys. Lett.*, vol 84, p. 2037, 2004

[58] K. Banerjee, S. Ghosh, E. Plis and S. Krishna, *Journ. of Electron. Materials*, vol. 39, p. 2210, 2010.

[59] E. Plis, J.B. Rodriguez, S.J. Lee and S. Krishna, *Electron. Lett.*, vol. 42, p. 1248, 2006.

[60] K. Banerjee, J. Huang, S. Ghosh, R. Xu, C. Takoudis, E. Plis, S. Krishna, S. Ketharanathan and M. Chriss, *Prco. of SPIE*, vol. 8012, p. 43, 2011

[61] O. Takahisa, *Surf. Sci.*, vol. 255, p. 229, 1991

[62] Z.Y. Liu, A.A. Gokhale, M. Mavrikakis, D.S. Saulys, and T.F. Kuech, *J. Appl. Phys.*, vol. 96, p. 4302, 2004.

CITED LITERATURE (continued)

[63] D.Y. Petrovykh, M.J. Yang, and L.J. Whitman, *Surf. Sci.*, vol. 523, p. 231, 2003.

[64] V.N. Bessolov and M.V. Lebedev, *Semiconductiors,* vol. 32, p.1141, 1998.

[65] P.S. Dutta, K.S. Sangunni, H.L. Bhat, and V. Kumar, *Appl. Phys. Lett.*, vol. 65, p. 1695, 1994.

[66] H. Oigawa, J.F. Fan, Y. Nannichi, H. Sugahara, and M. Osofhima, *Jpn. J. Appl. Phys.*, vol. 30, p. L322, 1991.

[67] S. Basu and P. Barman, *J. Vac. Sci. Technol. B,* vol. 10, p. 1078, 1992.

[68] M. Perotin, P. Coudray, L. Gouskov, H. Luquet, C. Linares, J.J. Bonnet, L. Soonckindt, and B. Lambert, *J. Electron. Mater*., vol. 23, p. 7, 1994.

[69] M.R. Ravi, A. Dasgupta, and N. Dasgupta, *IEEE T. Electron Dev.*, vol. 50, p. 532, 2003.

[70] P.S. Dutta, J. Langer, V. Bhagwat, and J. Juneja, *Proc. SPIE,* vol. 5783, p. 98, 2005.

[71] J. Li, S. Chuang, O. Sulima, and J. Cox, *J. Appl. Phys.*, vol. 97, p. 104506, 2005.

[72] J. Hoffmann, T. Lehnert, D. Hoffmann, and H. Fouckhardt, *Semicond. Sci. Tech.*, vol. 24, p. 065008, 2009.

[73] S. Mou, J.V. Li, and S.L. Chuang, *J. Appl. Phys.*, vol. 102, p. 066103, 2007.

CITED LITERATURE (continued)

[74] G. Aad, B. Abbott, J. Abdallah, A.A. Abdelalim, A. Abdesselam, O. Abdinov, B. Abi, *The Eur. Phys. Journ. C*, vol.70, p. 823, 2010

[75] A. Rimoldi, A. Dell'Acqua, M. Gallas, A. Nairz, J. Boudreau, V. Tsulaia, and D. Costanzo, *Nu. Sci. Symp. Con.*, vol. 3, pp. 1886, 2004.

[76] S. Michael, *Sol. Energ. Mat. Sol. C.*, vol. 87, p. 771, 2004.

[77] S. Michael and P. Michalopoulos, *45th Midwest Symposium on Circuits and Systems*, pp. II-651, 2002.

[78] P.R. Palmer, E. Santi, J.L. Hudgins, X. Kang, J.C. Joyce, P. Y. Eng, *IEEE T. Power Electr.*, vol. 18, p. 1220, 2003.

[79] S.K. Mandal, S. Chakraborty and C.K. Maiti, *Microelectron. Eng.*, vol. 81, p. 206, 2005.

[80] H.T Lim, F. Udrea, D.M. Garner, and W.I. Milne, *Solid State Electron.*, vol. 43, p. 1267, 1999.

[81] Y. Choi, K. Asano, N. Lindert, V. Subramanian, T. King, J. Bokor, C. Hu, *IEDM Technical Digest International Electron Devices Meeting*, p. 919, 1999.

[82] M. Ito, T. Kaneda, K. Nakajima, Y. Toyama, and H. Ando, *Solid State Electron.*, vol. 24, p. 421, 1981.

CITED LITERATURE (continued)

[83] K. Abu El-Rub, C.H. Grein, M.E. Flatte and H. Ehrenreich, *J. Appl. Phys.*, vol. 92, p.3771, 2002

[84] Q. K. Yang, F. Fuchs, J. Schmitz, and W. Pletschen, *Appl. Phys. Lett.*, vol. 81, p. 4757, 2002.

[85] C. Cervera, J.P. Perez, R. Chaghi, J.B. Rodriguez, P. Christol, L. Konczewicz and S. Contreras, *Journal of Physics: Conference Series*, vol. 193, p. 012030, 2009.

[86] K. Banerjee, S. Ghosh,S.Mallick, E.Plis, and S.Krishna, *J. Elec. Mat.*, vol. 38, p. 1944, 2009.

[87] D. Donetsky, S. P. Svensson, L. E. Vorobjev, and G. Belenky, *Appl. Phys. Lett.*, vol. 95, p. 212104, 2009.

[88] E. Plis, S. J. Lee, Z. Zhu, A. Amtout, and S. Krishna, *IEEE J. Sel. Top. Quant.*, vol. 12, p. 1269, 2006

[89] M.C. Teich, K. Matsuo, and B. E. A. Saleh, *IEEE J. Quantum Electron.*, vol. 22, pp. 1184, 1986.

[90] Y. Okuto and C. R. Crowell, *Phys.Rev. B*, Vol 10, p. 4284, 1974.

[91] S. Mallick, K. Banerjee, J.B. Rodriguez, S. Krishna, and S. Ghosh, *Appl. Phys. Lett.*, vol. 91, p. 241111, 2007.

CITED LITERATURE (continued)

[92] K. Banerjee, S. Ghosh, S. Mallick, E.Plis, S. Krishna, and C.Grein, *Appl. Phys. Lett.*, vol. 94, p. 201107, 2009.

[93] M. M. Hayat, O-H. Kwon, S. Wang, J. C. Campbell, B. E. A. Saleh, and M. C. Teich, *IEEE T. Elec. Dev.*, vol. 49, p. 2114, 2002.

[94] F. Capasso, W. T. Tsang, A. L. Hutchinson, and G. F. Williams, *Appl. Phys. Lett.*, vol. 40, p. 38, 1982

[95] J.C. Campbell, A. G. Dentai, W. S. Holden, and B. L. Kasper, *Elec. Lett.*, vol. 19, p. 818, 1983.

[96] K.A. Anselm, H. Nie, C. Hu, C. Lenox, P. Yuan, G. Kinsey, J. C. Campbell, and B. G. Streetman, *IEEE J. Quant. Elec.*, vol. 34, p. 482, 1998

[97] J. Beck, C. Wan, M. Kinch, J. Robinson, P. Mitra, R. Scritchfield, F. Ma, and J. Campbell, *J. Elec. Mat.*, vol. 35, p. 1166, 2006.

[98] F. Capasso, *Elec. Lett.*, vol 18, p. 12, 1982.

[99] J. Huang, K. Banerhee, S. Ghosh, and H.M. Hayat, *IEEE T. Elec. Dev.*, vol. 60, p. 2296, 2013.

APPENDIX

Electrical Characterization of Superlattice APDs

Electrical characterization of superlattice avalanche photodiodes in the research contains current-voltage and excess noise characterization. Janis ST-500-1-4LF mciromanipulated probe station was used as chamber for superlattice devices. The probe station as shown in Figure 22 has an insulated chuck, a mechanical oil pump, an air pressure gauge, a temperature controller and a Nitrogen dewar.

In current-voltage characterization, Agilent 4156B is the instrument for the measurement. Usually, current-voltage characteristics are measured in a low-temperature, high vacuum environment. First, samples are loaded into the chuck with grease at the bottom to ensure the thermal contact. Then, chamber was secured and vacuumed to at least 10^{-3} torr by the oil pump. During this process, it was monitor by air pressure gauge. After that, liquid nitrogen from dewar was used to cool down the whole chamber with the lowest temperature at 77K. It was pressurized with high-pressure dry nitrogen gas. Temperature controller were used to monitor the temperature. When the temperature arrived the set value, the controller would stabilize this temperature. It is recommended that extra time should be waited until the chamber really achieves target temperature. Probe station used two probes to touch the metal pads in the devices and connect to Agilent 4156B with two BNC cables. Extra care might be needed since the BNC cables might have charge and release currents at the moment of plugging into the circuit, wait time in Agilent 4156B

APPENDIX (continued)

can be setted to eliminate this interference. The source-monitor unit (SMU) ports were used for the measurement. Force and sense terminals of each SMU port were shorted before routing the combined connection to the probe station. The force terminal was used to set different voltage levels while the sense terminal measured the output current. During the measurement, light condition is critical since the photodiodes are sensitive to the light especially the infrared wave. Complete darkness is required during the measurement of dark current. Laser of certain wavelength with fixed power is used to initiate electrons and holes inside devieces for avalanche process. The experimental setup is shown in Figure 22. After the measurement, the data was saved to the disk in Agilent 4156B and then exported to computers for further graphing and calculations of dynamic resistance and multiplication gain.

APPENDIX (continued)

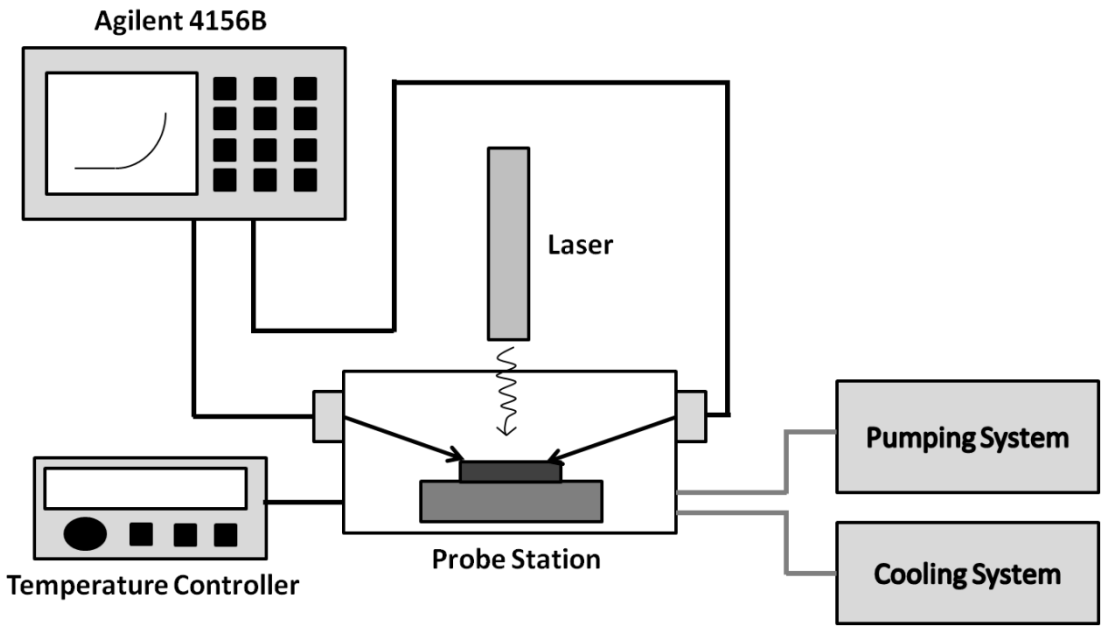

Figure 22 Experimental setup for current-voltage measurements

For the excess noise measurement, the noise figure analyzer Agilent 8973B was used. The excess noise setup is displayed in Figure 23.First, the photodiode device was biased at a reverse voltage with a particular multiplication gain using Agilent 4156B. Agilent 8973B was calibrated by a smart noise source Agilent N4001A. The output current was separated into DC and RF parts. Agilent 8973B is connected to its RF part with a center frequency of 10 MHz or 30 MHz and the bandwidth of 4 MHz. Powers are measured with and without illumination for the device with

APPENDIX (continued)

certain reverse bias. Under zero bias, the difference of these two powers were considered as reference without any multiplication noise included. Under higher bais, the difference of these two powers, minus the reference noise power would be the multiplication noise at this given bias value. And the excess noise factor could be calculated.

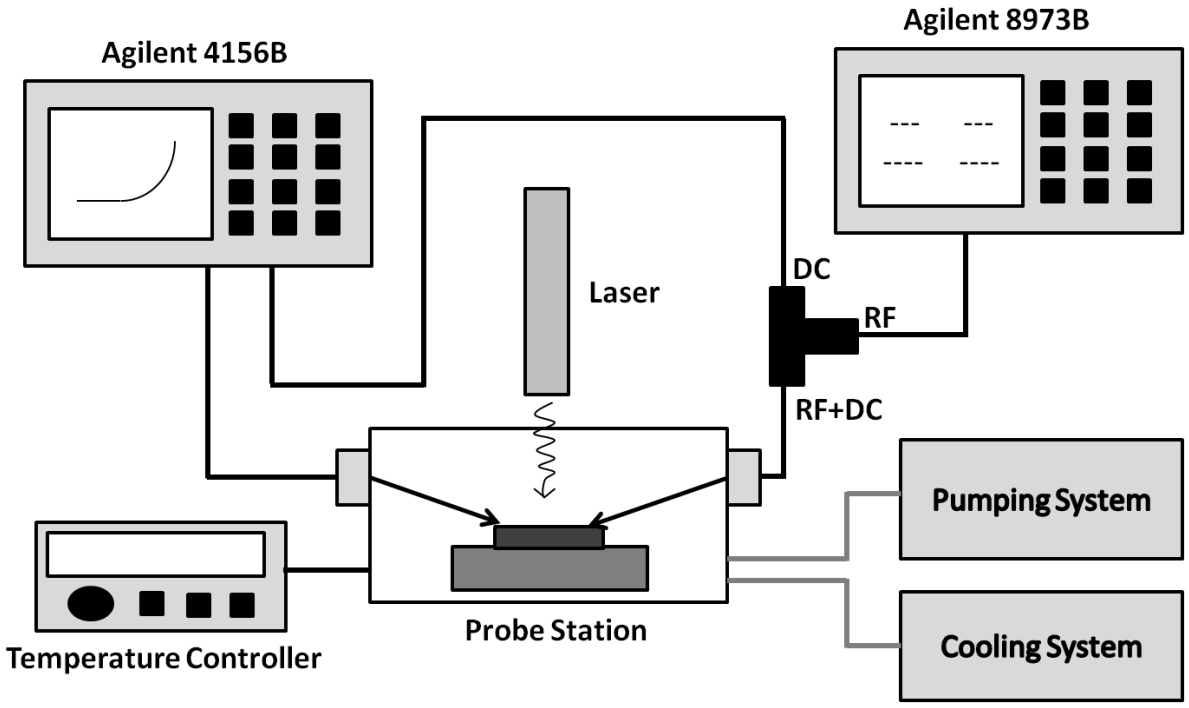

Figure 23 Experimental setup for excess noise measurements

VITA

NAME JUN HUANG

EDUCATION
PhD, University of Illinois at Chicago, 2015
MS, University of Illinois at Chicago, 2013
MS, University of Chicago, 2014
BS, Nanjing University of Science and Technology, 2009

EXPERIENCE
Summer Intern at Fairchild Semiconductors, 2013
Research Assistant in Electrical and Computer Engineering Department, 2010-2011
Teaching Assistant in Electrical and Computer Engineering Department, 2009-2015

AFFILIATIONS IEEE Student Member, IEEE Computer Society Student Member

PUBLICATIONS

J. Huang, K. Banerjee, S. Ghosh, and M.M. Hayat, "Dual-Carrier High-Gain Low-Noise Superlattice Avalanche Photodiodes." *Electron Devices, IEEE Transactions*, vol. 60, p. 2296, 2013.

J. Huang, K. Banerjee, S. Ghosh, M. Hayat, "Improved Dual-Carrier High Gain Strained Layer Superlattice Impact Ionization Engineered Avalanche Photodiode", *70th Device Research Conference*, p. 61, 2012

M. Purahmad, J. Huang, M. Plakhotnyuk, X. Zhang, J. Lee, A. Behranginia, P. Yasaei et al. "A MEMS-based resistive vacuum gauge with voltage readout." *26th International Vacuum Nanoelectronics Conference*, p. 1, 2013.

E. Hendries, J. Huang, R. Li, X. Li, Y. Qi, H. Sajer, S.M. Taylor, and J. Zerolis. "Bayesian Value at Risk Metric for Equity Portfolios." *SSRN 2490240*, 2014.

Y. Chang, C.R. Becker, C.H. Grein, S. Sivananthan, J. Huang, S. Ghosh, "Reduced Leakage Current of CdZnTe Radiation Detectors with HgTe/HgCdTe Superlattice Contacts", *Proc. SPIE*, vol. 8507, p. 15, 2012

K. Banerjee, J. Huang, S. Ghosh, "Modeling and simulation of long-wave infrared InAs/GaSb strained layer superlattice photodiodes with different passivants*", Infrared Physics &Technology*, vol. 54, p. 460, 2011

VITA (continued)

R. Xu, J. Huang, S. Ghosh, C.G. Takoudis, "Deposition and Characterization of Atomic Layer Deposited ZnS Thin Films on p-type GaSb (100) Using Diethylzinc Precursor and Hydrogen Sulfide", *ECS Transactions*, vol. 41, p. 229, 2011

K. Banerjee, J. Huang, S. Ghosh, R. Xu, C.G. Takoudis, E. Plis, S. Krishna, S. Ketharanathan, M. Chriss, "Surface study of thioacetamide and zinc sulfide passivated long wavelength infrared type-II strained layer superlattice", *Proceedings of SPIE*, vol. 8012, p. 43, 2011

K.G. Punchihewa, E. Zaker, R. Kuljic, J. Huang, K Banerjee, T Dankovic, A Feinerman, H Busta, etc, "Improvement of the sensitivity and operating range of MEMS-based resistive-type vacuum gauges", *24th International Vacuum Nanoelectronics Conference (IVNC)*, p. 191, 2011